JAMES | Journal of Advances in Modeling Earth Systems

RESEARCH ARTICLE
10.1029/2021MS002971

Improving Global Weather Prediction in GFDL SHiELD Through an Upgraded GFDL Cloud Microphysics Scheme

Linjiong Zhou[1,2], Lucas Harris[2], Jan-Huey Chen[2,3], Kun Gao[1,2], Huan Guo[2], Baoqiang Xiang[2,3], Mingjing Tong[2], J. Jacob Huff[2,3], and Matthew Morin[2,3]

[1]Program in Atmospheric and Oceanic Sciences, Princeton University, Princeton, NJ, USA, [2]National Oceanic and Atmospheric Administration/Geophysical Fluid Dynamics Laboratory, Princeton, NJ, USA, [3]University Corporation for Atmospheric Research, Boulder, CO, USA

Key Points:

- The Geophysical Fluid Dynamics Laboratory (GFDL) cloud microphysics scheme (GFDL MP) has been thoroughly updated for better physical realism and consistency
- The upgraded GFDL MP significantly improves large-scale weather prediction within the GFDL System for High-resolution prediction on Earth-to-Local Domains model
- Changes to the particle size distributions and cloud droplet number concentrations show significant impacts on weather prediction

Supporting Information:

Supporting Information may be found in the online version of this article.

Correspondence to:

L. Zhou,
Linjiong.Zhou@noaa.gov

Citation:

Zhou, L., Harris, L., Chen, J.-H., Gao, K., Guo, H., Xiang, B., et al. (2022). Improving global weather prediction in GFDL SHiELD through an upgraded GFDL cloud microphysics scheme. *Journal of Advances in Modeling Earth Systems*, *14*, e2021MS002971. https://doi.org/10.1029/2021MS002971

Received 24 DEC 2021
Accepted 23 JUN 2022

Abstract We describe the third version of the Geophysical Fluid Dynamics Laboratory cloud microphysics scheme (GFDL MP v3) implemented in the System for High-resolution prediction on Earth-to-Local Domains (SHiELD). Compared to the GFDL MP v2, the GFDL MP v3 is entirely reorganized, optimized, and modularized into functions. The particle size distribution (PSD) of all hydrometeor categories is redefined to better mimic observations, and the cloud droplet number concentration (CDNC) is calculated from the Modern-Era Retrospective analysis for Research and Applications, version 2 (MERRA2) aerosol data. In addition, the GFDL MP has been redesigned so all processes use the redefined PSD to ensure overall consistency and easily permit the introduction of new PSDs and microphysical processes. A year's worth of global 13-km, 10-day weather forecasts were performed with the new GFDL MP. Compared to the GFDL MP v2, the GFDL MP v3 significantly improves SHiELD's predictions of geopotential height, air temperature, and specific humidity in the Troposphere, as well as the high, middle and total cloud fractions and the liquid water path. The predictions are improved even further by the use of reanalysis aerosol data to calculate CDNC, and also by using the more realistic PSD available in GFDL MP v3. However, the upgrade of the GFDL MP shows little impact on the precipitation prediction. Degradations caused by the new scheme are discussed and provide a guide for future GFDL MP development.

Plain Language Summary Weather and climate models represent "microphysical" (MP) cloud and precipitation processes by assuming a certain distribution of particle sizes and then computing how the distributions affect transformations of one type of particle (cloud droplets, raindrops, ice crystals, snowflakes, etc.) into another. These schemes also assume the concentrations of the particulate matter (both naturally-occurring and human-made, such as soot, sulfate, dust, sea salt, etc.) onto which water condenses or ice freezes. One scheme that we use for global weather prediction, the Geophysical Fluid Dynamics Laboratory cloud microphysics scheme, has been recently upgraded to improve the consistency and realism of these processes, including more realistic cloud droplet size distributions, and use a more accurate time-and-space count of sulfate particles to calculate the number of cloud droplets. We find that this upgrade significantly improves global weather predictions, especially of the large-scale weather patterns and their clouds and precipitation.

1. Introduction

Clouds play critical roles in the weather conditions and in the global energy and water budgets that regulate the climate of the Earth (Houze, 2014; Lamb & Verlinde, 2011). The formation and evolution of clouds have significant impacts on precipitation forecasts in numerical weather prediction (Baldauf et al., 2011; Bauer et al., 2015; Morrison & Grabowski, 2008; Seifert & Beheng, 2005). Clouds-radiation interactions are among the most challenging aspects of climate modeling (Stephens et al., 2012; Trenberth et al., 2009; Wild et al., 2019). Making progress on any of these problems requires improving the representation of clouds in atmospheric models, which in nearly all practical weather and climate models is done through bulk microphysical parameterization (Kogan, 2013; Morrison & Gettelman, 2008; Nogherotto et al., 2016).

The Global Forecast System (GFS) at the National Centers for Environmental Prediction (NCEP) used the prognostic cloud microphysics scheme developed by Zhao and Carr (1997) from 1995 to 2019. Improving upon the very simple large-scale saturation adjustment scheme (Hoke et al., 1989) used in the early versions of GFS, this

computationally-inexpensive prognostic cloud microphysics scheme explicitly calculates a single cloud condensate species (Zhao et al., 1997) and uses a diagnostic partitioning between liquid and ice content and of precipitation. Forecasts using the Zhao and Carr (1997) scheme instead of the Hoke et al. (1989) diagnostic scheme improved the forecast skill of precipitation and reduced root-mean-square errors of specific humidity below 800 hPa and above 500 hPa (Zhao et al., 1997). However, the oversimplified treatment of cloud water and cloud ice excludes many microphysical processes and limits the realism and accuracy of cloud predictions and latent heating.

As computational resources have expanded in recent decades, more sophisticated cloud microphysics schemes have been developed and used in weather and climate models. Some studies have shown that by using a more comprehensive cloud microphysics scheme, one can achieve better weather prediction and climate simulation (Guo et al. (2021), Khain et al. (2015) and references therein). In 2010, the European Centre for Medium-Range Weather Forecasts (ECMWF) replaced the ancient Tiedtke (1993) scheme with the elegant Forbes and Tompkins (2011), Forbes et al. (2011) prognostic scheme for the Integrated Forecast System (IFS). The National Center for Atmospheric Research upgraded the Rasch and Kristjánsson (1998) prognostic condensate and precipitation scheme to the well-known Morrison and Gettelman (2008) scheme for the Community Atmosphere Model version 5 in 2012. The Geophysical Fluid Dynamics Laboratory (GFDL) also implemented this scheme into the GFDL AM4 climate model (Guo et al., 2021) replacing the simpler Rotstayn-Klein cloud microphysics scheme (Jakob & Klein, 2000; Rotstayn, 1997; Rotstayn et al., 2000). After extensive evaluation, NCEP chose to replace the Zhao and Carr (1997) cloud microphysics scheme with the GFDL cloud microphysics scheme (GFDL MP), used in GFDL's weather prediction models (Chen & Lin, 2013; Zhou et al., 2019), in the GFS upgrade of June 2019. The goal of this upgrade was to improve weather prediction through a better representation of microphysical processes.

The GFDL MP is a five-category, single-moment bulk microphysics scheme originally designed for improved simulation of weather systems, extreme events (especially tropical cyclones), and atmospheric variability. The GFDL MP predicts two liquid categories (cloud water and rain) and three ice categories (cloud ice, snow, and graupel or hail). Zhou et al. (2019) and Harris, Zhou, et al. (2020) have described key features of the GFDL MP, including thermodynamic consistency with the dynamical core, fast and stable sedimentation processes, and tight coupling between dynamics and physics. The GFDL MP is used in the operational GFS version 15 and 16 (Huang et al., 2021; Patel et al., 2021; Tong et al., 2020) and several other weather and climate models, including GFDL radiative-convective equilibrium (RCE) simulations within a limited domain (Jeevanjee, 2017), the GFDL High-resolution Atmosphere Model (HiRAM; Chen and Lin (2011), Chen and Lin (2013), Gao et al. (2017, 2019), Harris et al. (2016)), the GFDL System for High-resolution prediction on Earth-to-Local Domains (SHiELD; Harris, Zhou, et al. (2020)), the National Oceanic and Atmospheric Administration's Hurricane Analysis and Forecast System (HAFS; Dong et al. (2020); Hazelton et al. (2021)), the Chinese Academy of Sciences Flexible Global Ocean-Atmosphere-Land System Model (He et al., 2019; Li et al., 2019; Zhou et al., 2015), and the National Aeronautics and Space Administration Goddard Earth Observing System (GEOS) version 5 (Arnold et al., 2020).

The principal development of the GFDL MP is within SHiELD at GFDL. Although the performance of SHiELD has gradually improved over the years with the continuous upgrades of the GFDL MP, cloud, precipitation, and radiation predictions are still challenging. For example, ice cloud fraction is under-predicted by about 12% and so the long-wave radiation at the top of the atmosphere is significantly over-estimated by about 8 $W\,m^{-2}$. Liquid cloud fraction is also significantly under-predicted over the global oceans. In addition, SHiELD tends to predict excessive light and extreme precipitation and under-predict medium precipitation (Harris, Zhou, et al., 2020). Khain et al. (2015), in a broad review of the literature, found that precipitation rate, type of precipitation (liquid or ice), and spatial distributions of precipitation in global forecast systems were found to be strongly dependent on the shape of the particle size distribution (PSD). In another review, Fan et al. (2016) found that aerosol-cloud interactions have significant impacts on radiative forcing, precipitation, extreme weather, and large-scale circulation. From this, we expect that improvements to the PSD and prescribed aerosol concentrations used by the GFDL MP could significantly improve simulation quality and prediction skills in these models.

This paper aims to document the most recent version 3 of the GFDL MP and understand its impacts on weather prediction skills and biases. In particular, we will describe the impacts of the more realistic PSD and the use of the time-and-space varying climatological aerosol for cloud droplet number concentration (CDNC) on large-scale

height, temperature, and humidity predictions, and on cloud and precipitation predictions. This paper will also serve as a reference for future model and parameterization development.

The rest of the paper is organized as follows. Section 2 briefly introduces the SHiELD model used in this study. Section 3 documents the upgrade of the GFDL MP in detail. Section 4 describes the model setup and experiments for this study. Section 5 presents the upgraded GFDL MP's impacts on weather prediction skills and biases. Section 6 demonstrates the impacts of the realistic PSD and the use of climatological aerosol for CDNC on weather prediction. Finally, we end with a summary and discussion in Section 7.

2. SHiELD Model Description

The model used in this study is the GFDL global weather model SHiELD. SHiELD, previously called fvGFS (finite-volume Global Forecast System; Chen, Lin, Magnusson, et al. (2019), Chen, Lin, Zhou, et al. (2019), Hazelton et al. (2018), Zhou et al. (2019)), was developed as a prototype of the Next-Generation Global Prediction System of the National Weather Service and the broader Unified Forecast System (UFS) (Harris, Zhou, et al., 2020). SHiELD focuses on medium-range weather (up to 10 days) prediction, but it can also be used for sub-seasonal to seasonal (S2S; between 2 weeks and one season) (Harris, Zhou, et al., 2020) and convective-scale (a few hours) (Harris et al., 2019) predictions as well. Notably, advances in SHiELD have migrated into UFS models slated for operational implementations at NCEP, including the GFS version 15 and version 16.

SHiELD uses the non-hydrostatic solver of the Finite-Volume Cubed-Sphere Dynamical Core (FV3) developed at GFDL (Harris & Lin, 2013; Harris, Zhou, Chen, & Chen, 2020; Harris, Chen, et al., 2020; Putman & Lin, 2007; S. Lin, 2004). The physical parameterizations in SHiELD originated from that in GFS version 14 (Chen, Lin, Magnusson, et al., 2019), but contains substantial updates: In particular the simple microphysics scheme of Zhao and Carr (1997) and cloud fraction scheme of Xu and Randall (1996) are replaced by the inline GFDL cloud microphysics (Harris, Zhou, et al., 2020; Zhou et al., 2019). We have also redesigned cloud-radiation interaction to combine the cloud microphysics processes and cloud radiative properties. To incorporate atmosphere-ocean interactions, we have implemented a mixed layer ocean based on Pollard et al. (1973). This simple ocean model calculates the mixed layer depth and temperature within that mixed layer as prognostic variables, driven by surface wind stress and heat fluxes from the atmosphere together with a nudging toward climatology applied to the mixed layer temperature and mixed-layer depth (Harris, Zhou, et al., 2020). In the version of SHiELD that is used in this paper, the convection schemes (Han et al., 2017), planetary boundary layer scheme (Han & Bretherton, 2019), and land surface model (Ek et al., 2003) are all updated to synchronize the current operational GFS version 16.

3. Cloud Microphysics Parameterization

The GFDL MP has its origins in an earlier scheme originally developed for seasonal hurricane prediction in HiRAM (Chen & Lin, 2013), which itself was based on the Y. Lin et al. (1983) taken from the GFDL ZETAC model (Pauluis & Garner, 2006). The first version of the GFDL MP (GFDL MP v1; Zhou et al. (2019)), was mainly developed to support the early versions of SHiELD and what became the FV3-based GFS version 15. This was a split cloud microphysics scheme in which the fast phase changes were built within the FV3 dynamical core. GFDL MP v1, with some minor upgrades, is still in use in the operational GFS version 16 and GFS ensemble version 12. GFDL MP v2 (Harris, Zhou, et al., 2020) was developed with an option to be run entirely within the FV3 dynamical core. For this reason, we call this capability "inline microphysics". Most recently, the GFDL MP in SHiELD has been dramatically updated and will be referred to as GFDL MP v3 because it is significantly different from the second version. Compared with the GFDL MP v2, the code of the GFDL MP v3 is entirely reorganized, optimized, and modularized into functions. All scientific updates are described in Appendix A.

The most significant updates in the GFDL MP v3 are the revised PSD and the overall physical consistency between processes. First, the PSDs for all five hydrometeor categories are redefined as a gamma distribution to mimic observed PSDs. As a result, the cloud water and cloud ice are no longer mono-dispersed as in the GFDL MP v2. The precipitation particles, for example, rain, snow, and graupel, or hail, still follow the exponential distribution as suggested by most observations and literature (Khain et al. (2015) and references therein), and which is a special case of the gamma distribution. Along with the revised PSD, all microphysical processes,

Table 1
The Intercept Parameter (n_0, Unit: $m^{-3-\mu}$), Spectral Shape Parameter (μ, Unit: 1), Density of Hydrometeor Category (ρ', Unit: kg m^{-3}), Parameter α (Unit: $m^{1-\beta}\ s^{-1}$) and β for Each Hydrometeor Category of the GFDL MP v3

	Cloud water	Cloud ice	Rain	Snow	Graupel	Hail
n_0	1.2×10^{66}	1×10^{10}	8×10^{6}	3×10^{6}	4×10^{6}	4×10^{4}
μ	11	1	1	1	1	1
ρ'	1×10^{3}	9.17×10^{2}	1×10^{3}	1×10^{2}	4×10^{2}	9.17×10^{2}
α	3×10^{7}	11.72	842	4.8	40.74	61.68445
β	2	0.41	0.8	0.25	0.5	0.5
D_{eff}	10–20	20–300	20–20,000	300–20,000	300–20,000	300–20,000
V	0–0.01	0–1	0–12	0–2	0–12	0–12

Note. The valid ranges of effective diameter (D_{eff}, unit: $\times 10^{-6}$ m) and terminal velocity (V, unit: $m\ s^{-1}$) are at the bottom of this table. Parameters n_0 and μ for cloud water, cloud ice, rain, snow, and graupel or hail are derived based on Martin et al. (1994), Fu (1996), Marshall and Palmer (1948), Gunn and Marshall (1958), and Houze et al. (1979) or Federer and Waldvogel (1975), respectively. Parameters α and β for cloud water, cloud ice, rain, snow, and graupel or hail follow Ikawa and Saito (1991), McFarquhar et al. (2015), Liu and Orville (1969), Straka (2009), and Pruppacher and Klett (2010), respectively.

including accretion, evaporation, sublimation/deposition, and freezing/melting, have been re-formulated to use the new PSD. This ensures microphysical consistency and easily permits introductions of new PSDs, microphysical processes, and multi-moment distributions. The details of these updates are described in the following subsection. Due to the introduction of the more realistic PSD and the reformation of many microphysical processes, the computational runtime of the microphysics scheme increases by about 20%, but only increases the total SHiELD runtime by about 2%. We feel this is an acceptable cost given the substantial skill improvements we describe below.

3.1. Particle Size Distribution (PSD)

The PSD describes the number concentration of a cloud particle as a function of the particle size. Common PSDs are mono-dispersed, exponential, gamma, or log-normal distribution (Straka, 2009). All cloud properties and cloud processes can then be computed by analytically integrating different products of the PSDs. In the GFDL MP v3, the PSD of each hydrometeor category is defined by a gamma distribution containing three parameters:

$$n(D) = n_0 D^{\mu-1} \exp(-\lambda D), \tag{1}$$

where n_0 ($m^{-3-\mu}$) is the intercept parameter, μ (unitless) is the spectral shape parameter, λ (m^{-1}) is the slope parameter, and D (m) is the particle diameter. When the spectral shape parameter μ equals 1, the gamma distribution becomes an exponential distribution. In a single-moment bulk cloud microphysics scheme with prognostic mass specific ratio q ($kg\ kg^{-1}$), the intercept parameter n_0 and spectral shape parameter μ are predefined constants, while the slope parameter λ can be derived from n_0, μ, and q. The values of n_0 and μ for each hydrometeor category of the GFDL MP v3 are listed in Table 1. Note that all hydrometeor categories are assumed as spherical particles in the GFDL MP.

The PSD depends on cloud content (ρq) or the mass specific ratio of cloud (q) through the slope parameter (λ, Equation B7). Figure 1 shows the particle size distributions used in the GFDL MP v3, including that cloud water droplet number, follows a gamma distribution while all other hydrometeor categories follow the exponential distribution. The particle numbers increase with cloud content increases at a fixed cloud diameter. Cloud water droplets (Figures 1a and 1b) have sizes between 6 and 40 μm, with a peak droplet number at around 20 μm. Cloud water droplet number is three orders of magnitude less when the cloud water content drops from 10 $g\ m^{-3}$ to 10^{-4} $g\ m^{-3}$. Following the exponential distribution, cloud ice particle number monotonically decreases as particle size increases (Figures 1c and 1d). The distributions of rain, snow, graupel, and hail particle numbers are similar (Figure 1e-1l), except that rain has the largest particle number while hail has the lowest particle number because rain (hail) has the highest (lowest) intercept parameter (n_0). Rain, snow, graupel, and hail particle numbers approach zero at diameter between 2000 to 6000 μm, depending on the specific species and water content. Very high water contents are needed to produce non-negligible numbers of the largest particles.

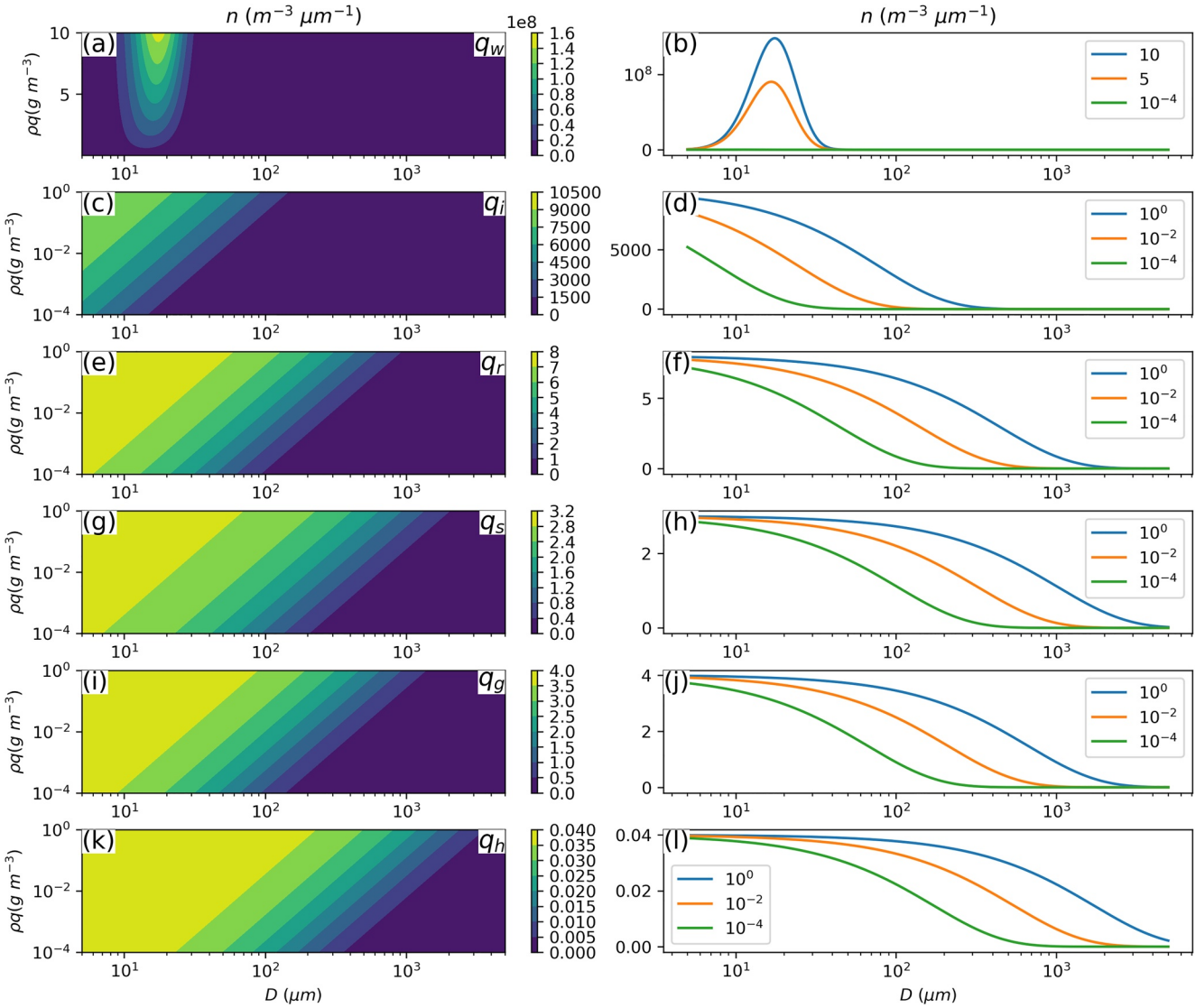

Figure 1. (a, c, e, g, i and k) particle size distribution (PSD) (n, unit: m^{-3} μm^{-1}) as a function of diameter (D, unit: μm) and cloud content (ρq, unit: $g\ m^{-3}$). (b, d, f, h, j and l) PSD as a function of diameter at three selected cloud water content amounts. (a and b) are cloud water (q_w), (c and d) are cloud ice (q_i), (e and f) are rain (q_r), (g and h) are snow (q_s), (i and j) are graupel (q_g), and (k and l) are hail (q_h).

While cloud ice particle number still follows the exponential distribution ($\mu = 1$) as in Fu (1996) that is used to calculate cloud ice radiative properties, recent studies (McFarquhar et al., 2015) find that cloud ice is found to follow the gamma distribution ($\mu > 1$). Development using the gamma distribution for cloud ice is ongoing.

Once the PSD is defined, we can derive the particle concentration (N), effective diameter (D_{eff}), optical extinction (β), mass specific ratio (q), radar reflectivity factor (Z), and terminal velocity (V) by integrating the PSD over all diameters. Details of calculating these quantities characterizing cloud parameters can be found in Appendix B. Since the PSDs are redefined, all cloud microphysical processes are reformulated accordingly to ensure overall microphysical consistency and easily permit future introductions of new PSD, microphysical processes, and multi-moment distributions. Details of the microphysical processes can be found in Appendix C.

How does the revised PSD for cloud particles affect the effective diameter and terminal velocity? The PSD of precipitation particles (e.g., rain, snow, graupel, or hail) remains the same from GFDL MP v2 to GFDL MP v3, but the PSD of cloud water and cloud ice has been changed from mono-dispersed distribution to gamma and exponential distributions, respectively. Figure 2 demonstrates the differences in effective diameter and terminal velocity between GFDL MP v2 and GFDL MP v3. The effective diameter of cloud water in GFDL MP v3 (solid

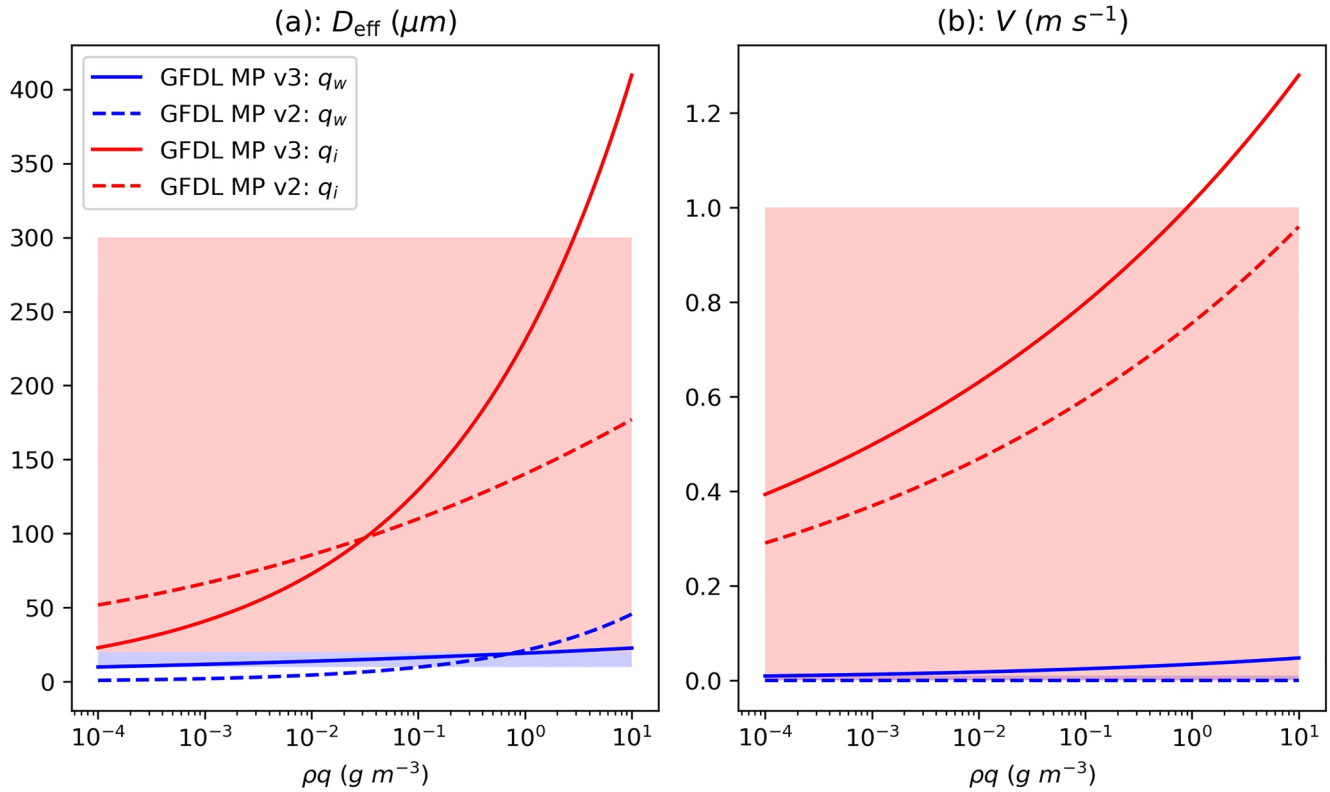

Figure 2. (a) Effective diameter (D_{eff}, unit: μm) and (b) terminal velocity (V, unit: $m\ s^{-1}$) as a function of cloud content (ρq, unit: $g\ m^{-3}$). Solids lines are D_{eff} or V computed from PSD in the GFDL MP v3; dashed lines are those empirically diagnosed in the GFDL MP v2. Blue lines represent cloud water; red lines represent cloud ice. Blue shaded area is the range limit of D_{eff} or V for cloud water; Red shared area is the range limit of D_{eff} or V for cloud ice.

blue line in 2a) mostly lies between 10 and 20 μm in the cloud content between 10^{-4} and 10^{1} $g\ m^{-3}$. However, the effective diameter of cloud water in GFDL MP v2 (dashed blue line in 2a) exhibits a larger gradient as a function of cloud content, leading to lower (higher) than the predefined range limit of cloud water effective diameter when there is little (much) cloud content. On the contrary, the gradient of cloud ice effective diameter in GFDL MP v2 (dashed red line in 2a) is smaller compared with the one in GFDL MP v3 (solid red line in 2a) and mostly inside the predefined range limit. Since a smaller cloud effective diameter produces a stronger radiative effect and vice versa, these results indicate a stronger shortwave radiative effect and a weaker longwave radiative effect when there is little cloud content, while a weaker shortwave radiative effect and a stronger longwave radiative effect when there is much cloud content. As for the terminal velocity, although the cloud water in GFDL MP v3 (sold blue line in 2b) has a greater value, most of which is capped by the predefined 0.01 $m\ s^{-1}$ upper bound. Since the terminal velocity of cloud water is very smaller compared to other hydrometeor categories, its impact on cloud prediction is neglectable. As for cloud ice, its terminal velocity in the GFDL MP v3 (solid red line in 2b) is about 0.2 $m\ s^{-1}$ larger than that in the GFDL MP v2 (dashed red line in 2b) in the cloud content between 10^{-4} and 10^{1} $g\ m^{-3}$. The difference in cloud ice terminal velocity will change cloud ice content prediction and cloud ice-involved microphysical processes, for example, accretion, deposition, and melting.

3.2. Cloud Droplet Number Concentration (CDNC)

Among all microphysical processes, cloud water to rain autoconversion (P_{aut}, unit: $kg\ kg^{-1}\ s^{-1}$) follows Manton and Cotton (1977):

$$P_{aut} = \frac{0.104 g E_{aut} \rho^{4/3}}{\upsilon (N_c \rho')^{1/3}} q^{7/3} H(q - q_c), \tag{2}$$

$$q_c = \frac{N_c}{\rho} \frac{4}{3} \pi \rho' R_c^3. \tag{3}$$

Here, $E_{aut} = 0.5$ is the collection efficiency, $\upsilon = 1.717 \times 10^{-5}$ m^2 s^{-1} is the dynamics viscosity of air, N_c (m^{-3}) is the CDNC, $R_c = 10 \times 10^{-6}$ m and q_c ($kg\ kg^{-1}$) are the critical mean cloud droplet radius and the mass mixing ratio respectively, and H is the Heaviside unit step function. Based on this equation, with the increase of N_c, the rate of the cloud water to rain autoconversion decreases, resulting in more cloud water and less rain, and vice versa. The GFDL MP does not explicitly perform droplet activation but instead directly uses the pre-calculated CDNC (N_c). For simplicity, the GFDL MP v2 only used two single fixed values of N_c over the land (300 cm^{-3}; Tripoli and Cotton (1980)) and over the ocean (100 cm^{-3}; Rotstayn (1997)), that the aerosol-related microphysical processes and the aerosol-cloud interactions cannot be properly represented.

In the GFDL MP v3, the aerosol data in the Modern-Era Retrospective analysis for Research and Applications, version 2 (MERRA2) (Rienecker et al., 2011) from the National Aeronautics and Space Administration (NASA) Goddard Earth Science Data Information and Services Center (GES DISC) is adopted. This aerosol product is one of the reanalyzes from the Goddard Earth Observing System Model, Version 5 (GEOS-5) data assimilation system (Gelaro et al., 2017; Randles et al., 2017). We combined the 3-hourly aerosol data from 2015 to 2020 to create a 12-month climatological data set consisting of 72 vertical levels from the surface to about 1.3 Pa at the top. The horizontal resolution is 0.5 by 0.625°. The species of sulfate, which is a subset of MERRA2 aerosol, is converted to CDNC using Boucher and Lohmann (1995)'s formula:

$$N_c = \begin{cases} 10^{2.24}\left(10^9 \rho q_a\right)^{0.257} \times 10^6 & \text{land,} \\ 10^{2.06}\left(10^9 \rho q_a\right)^{0.480} \times 10^6 & \text{ocean.} \end{cases} \tag{4}$$

where q_a (unit: $kg\ kg^{-1}$) is the mass specific ratio of sulfate aerosol from MERRA2.

Figures 3a and 3b show the geographic distribution of surface climatological CDNC derived from MERRA2 and its difference from the values used in the GFDL MP v2 (300 and 100 cm^{-3} over the land and the ocean, respectively). In most of the land area except for southeastern China and northern India, the CDNC from MERRA2 is below 300 cm^{-3}. The CDNC in Antarctica is below 100 cm^{-3}. Over most of the ocean area except for the offshore of Asia and Europe, the east coast of North America, and the northern Pacific Ocean, the CDNC from MERRA2 is below 100 cm^{-3}. Only the CDNC around the offshore of China and India can reach above 300 cm^{-3}. The above comparison indicates that the fixed values of CDNC used in the GFDL MP v2 are substantially overestimated in most areas of the globe. Besides the horizontal variability, the MERRA2 CDNC also changes vertically and with seasonal variation. Figure 3c shows that the vertical mean distributions and ranges are decreasing with height, and the values are much smaller than the fixed values used in the GFDL MP v2. The CDNC in the land is only about 150 cm^{-3} near the surface, and it could be lower than 100 cm^{-3} above 500 hPa. The CDNC over the ocean is generally half value or less than the fixed value of 100 cm^{-3}. From Figure 3d, we can see that the maximum (minimum) surface CDNC shows in the winter (summer) regardless of surface type. Noticeable seasonal variation is found in the Amazon Basin, Europe, India, East Asia and its surrounding ocean, and over the Southern Ocean (see Figure S1 in Supporting Information S1). The impact of the seasonal cycle of CDNC on weather prediction will be discussed in the following sections.

4. Model Setup and Experiments

In order to demonstrate the impact of the GFDL MP upgrade, we evaluate a suite of 10-day weather predictions using SHiELD. These predictions are initialized from the operational GFS v15 analyses every five days from 25 June 2019 to 17 March 2021 (124 individual 10-day forecasts). The current version of SHiELD does not include data assimilation, so the initial conditions are from the operational GFS analysis. The ERA5 reanalysis (Hersbach et al., 2020) is then used for the global weather prediction evaluation. ERA5 is produced using 4D-Var data assimilation and model forecasts in CY41R2 of the ECMWF IFS, with 137 hybrid sigma/pressure (model) levels in the vertical and the top-level at 0.01 hPa. Here the 31-km 6-hourly ERA5 datasets at the pressure levels of 100, 200, 250, 500, 700, 850, and 1000 hPa are used to represent the weather and atmospheric condition from Tropopause to the surface. Here we focus on geopotential height, air temperature, and specific humidity, which are used to demonstrate the model's capability for large-scale weather prediction.

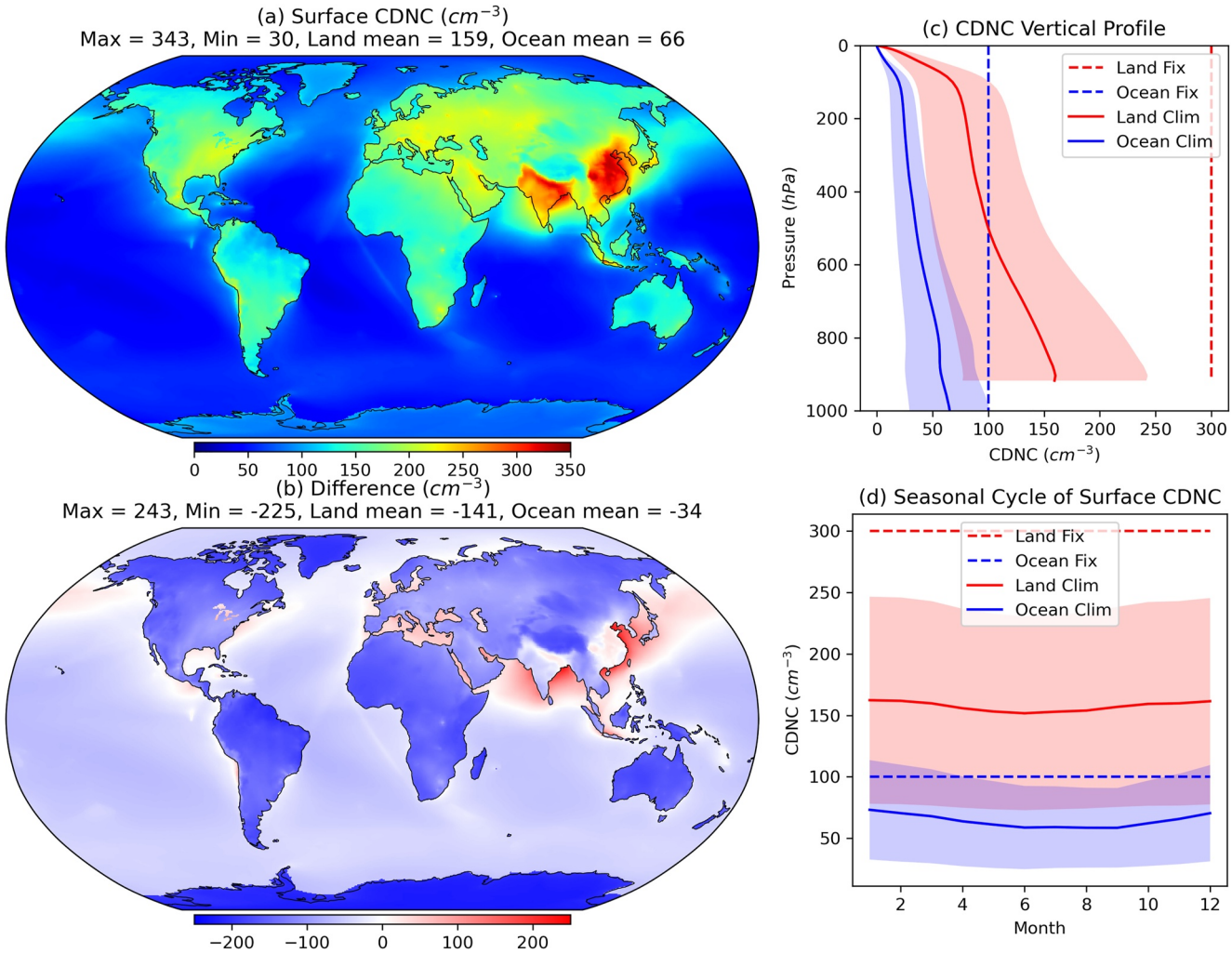

Figure 3. Geographic distribution of (a) surface climatological cloud droplet number concentration (CDNC) (cm^{-3}) calculated from Modern-Era Retrospective analysis for Research and Applications, version 2 (MERRA2), (b) the difference between the CDNC from MERRA2 and the fixed CDNC values used in the GFDL MP v2. Panel (c) is the vertical profiles of climatological CDNC from MERRA2 (solid) and fixed CDNC values used in the Geophysical Fluid Dynamics Laboratory cloud microphysics scheme (GFDL MP) v2 (dashed). Panel (d) is the seasonal cycle of climatological surface CDNC from MERRA2 (solid) and fixed CDNC values used in the GFDL MP v2 (dashed). Red lines represent CDNC in the land area, blue lines represent CDNC over the ocean. The shaded area is its standard deviation. The numbers in panels (a and b) are the global maximum, minimum, land mean, and ocean means of CDNC.

To comprehensively evaluate the cloud prediction, version 2 of COSP (Cloud Feedback Model Intercomparison Project Observation Simulator Package; Swales et al. (2018)) has been recently implemented into SHiELD. The COSP simulates the retrievals for several passive and active sensors by using the model data (e.g., cloud water content at model levels). Therefore, we can directly compare the output from COSP of SHiELD against CALIPSO (Cloud-Aerosol Lidar and Infrared Pathfinder Satellite Observation; Bodas-Salcedo et al. (2011), Chepfer et al. (2010)) cloud fraction product. The total column of cloud liquid water, rainwater, cloud ice water, and snow water from ERA5 is also used to evaluate the liquid and ice water paths predicted in SHiELD. Note that graupel is not included in ERA5. For both SHiELD and ERA5, the total column cloud liquid water and the rainwater are combined as the liquid water path, and the total column cloud ice water and the snow water are combined as the ice water path. The model's precipitation prediction is evaluated against the Integrated Multi-satellitE Retrievals for GPM (IMERG) product (Hong et al., 2004), which combines information from the Global Precipitation Measurement (GPM) satellite constellation to estimate precipitation over the majority of the Earth's surface.

Table 2
List of Experiments in This Study

Experiment	New PSD[a]	New CDNC[b]	GFDL MP
OLD			v2
CTRL			v3
CPSD	×		v3
AERO		×	v3
CPSD_AERO	×	×	v3

[a]gamma distribution for cloud water and exponential distribution for cloud ice. [b]CDNC are calculated from climatological aerosol.

Table 2 listed all experiments done for this study. OLD used GFDL MP v2 with constant CDNCs over the land and ocean respectively and the original PSD for all hydrometeor categories. CTRL used GFDL MP v3 with the same PSD and CDNC as OLD. The comparison between CTRL and OLD shows the impact of code updates and scientific updates described in Appendix A. In the following section, CTRL is used as a reference to evaluate the weather prediction skill of the GFDL MP v3. In particular, CTRL is compared against simulations with the more realistic PSD of cloud water and cloud ice (CPSD), a time-and-space varying climatological background aerosol for CDNC calculation (AERO), and simulations with both (CPSD_AERO).

5. Model Verification

Figure 4 shows a straightforward comparison between OLD and CTRL on a scorecard. It shows that CTRL has significantly higher anomaly correlation coefficients (ACCs) of geopotential height at most pressure levels up to 7 days of forecast. The reduction of geopotential height bias from OLD to CTRL is significant throughout the 10 days of forecast. Although the ACCs of CTRL are lower than those of OLD after day seventh, this difference is insignificant. The above improvement of geopotential height prediction (higher ACC of geopotential height) is encouraging for the development of SHiELD because it indicates a general improvement of the atmospheric circulation and heating in the Troposphere, which is closely related to our daily weather. It is also found in Figure 4 that the temperature prediction of CTRL is generally better than OLD. Still, the ACCs are higher in the first few days and lower in the eight to 10-day forecast, while the bias is significantly reduced during the entire 10-day forecast. Unfortunately, temperature prediction at 500 hPa and 1000 hPa are degraded in CTRL (shown as lower ACCs and larger biases). Further analyses on the 10-day temperature evolution and its 10-day averaged geographical distribution (see supplemental Figures S2 and S3 in Supporting Information S1) show a globally warm bias at 500 hPa and 1000 hPa. Since CTRL predicts a generally warmer Troposphere than OLD and the 500 hPa and 1000 hPa temperature in OLD already have a positive bias, the additional warming further increases the positive bias at these two pressure levels. From the scorecard, the specific humidity prediction is generally better in the upper Troposphere but worse in the lower Troposphere when comparing CTRL to OLD. However, compared to the magnitude and variation of specific humidity during the 10 days of forecasts, their difference at the lower Troposphere is relatively small and could be negligible (see Figures S2 and S3 in Supporting Information S1).

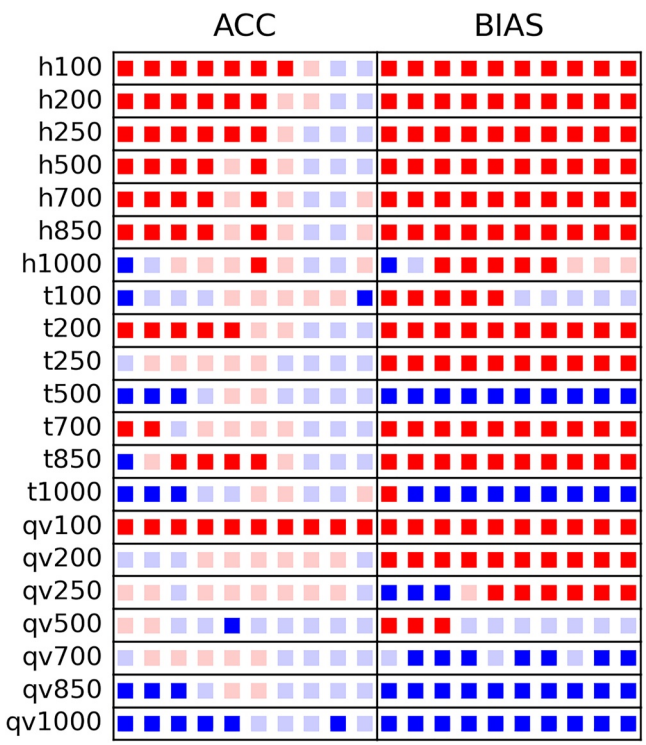

Figure 4. The scorecard showing the comparisons between the Geophysical Fluid Dynamics Laboratory cloud microphysics scheme (GFDL MP) v3 (CTRL) and the GFDL MP v2 (OLD) in each meteorological field. Improvements (degradation) from CTRL are indicated in red (blue) squares, for example, higher (lower) anomaly correlation coefficient (ACC) or less (larger) bias. Darker colors mean the difference passes the 95% significance level. Square boxes in each grid cell from left to right are for the forecasts from day 1 to day 10. The letters h, t, and qv to the left represent geopotential height, temperature, and specific humidity, respectively, at pressure levels of 100, 200, 250, 500, 700, 850, and 1000 hPa.

Figure 5 shows the cloud fraction comparison between model prediction and CALIPSO observation. In Figure 5e, we can see that OLD predicts similar geographical distribution and magnitude of high cloud fraction as CALIPSO. The predicted global mean high cloud fraction is slightly smaller than that of the CALIPSO (with a bias of −0.006). As shown in Figure 5i, the global mean bias further reduces to 0.001 (positive) in CTRL, but the root-mean-square error (RMSE) remains the same (0.103). It can be found in the high cloud fraction difference panel (Figure 5m) that there is a significant difference in high cloud fraction over the tropics ocean area. Different from the high cloud fraction, both middle and low cloud fractions are under-predicted in either OLD or CTRL (Figure 5f, 5g, 5j and 5k). As shown in Figures 5f and 5j, the predicted middle cloud fraction is consistently lower in the model than CALIPSO, with a maximum reduction of cloud fraction in Southern America (also see Figure S4 in Supporting Information S1). Comparing OLD and CTRL, the upgrade of GFDL MP only improves some of the middle cloud

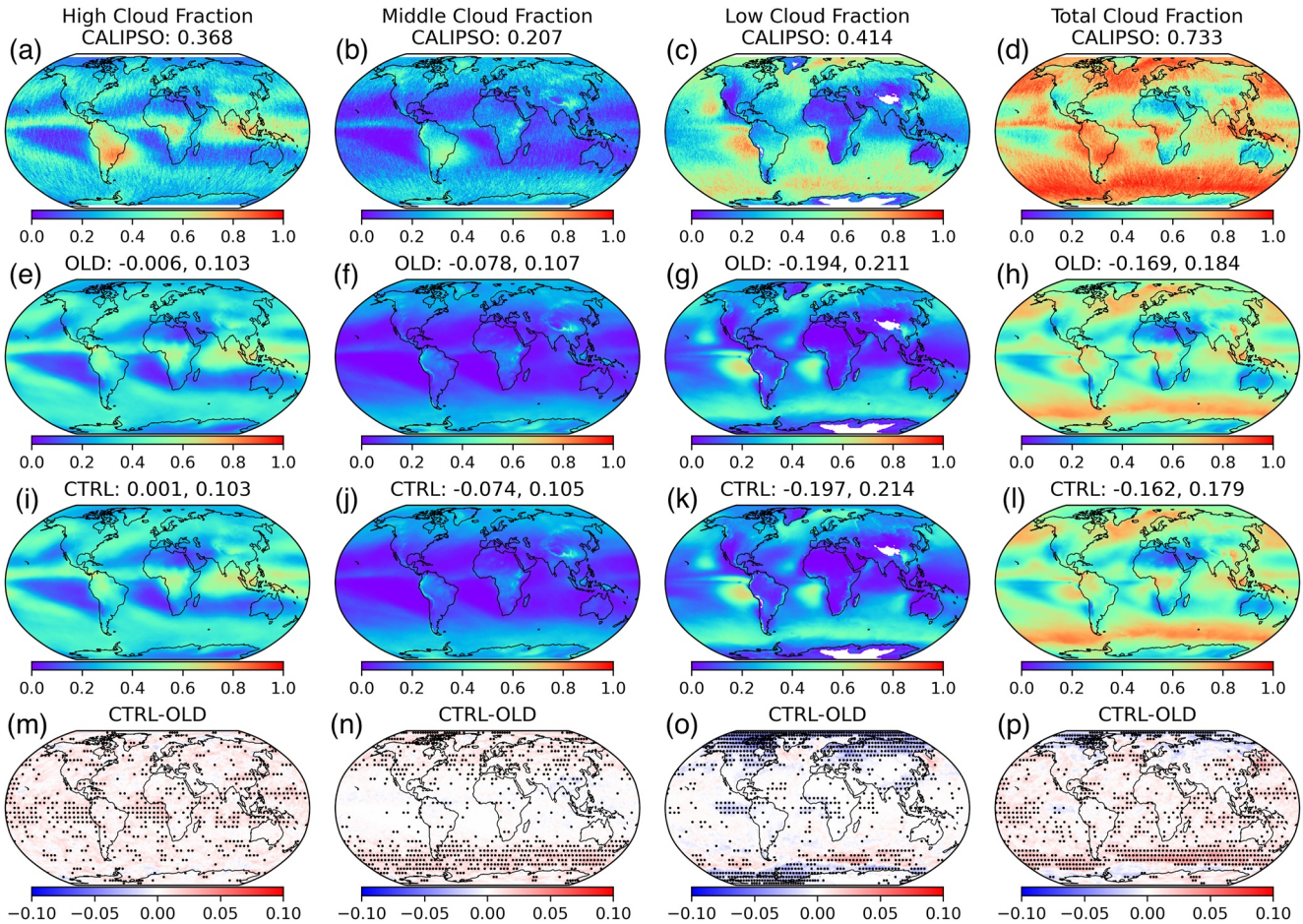

Figure 5. From left to right are the 10-day averaged high, middle, low, and total cloud fractions from (a–d) Cloud-Aerosol Lidar and Infrared Pathfinder Satellite Observation (CALIPSO), (e–h) OLD, (i–l) CTRL, and (m–p) CTRL minus OLD. The numbers in the title of (a–d) are the global mean of cloud fraction (unitless), and (e–l) are the bias and root-mean-square error compared to CALIPSO. The dotted area in (m–p) is the area with a 95% significant difference.

fraction prediction, with the reduced global mean bias and RMSE. As shown in Figure 5n, most of the significant middle cloud fraction increment is over the ocean area in the middle to high latitude, especially over the Southern Ocean. The change of high cloud fraction in the tropics and middle cloud fraction in the middle to high latitude, where consists of a majority of ice cloud, is mainly due to the update of supersaturation calculation in the ice processes as described in Appendix A. Compared to the middle cloud fraction bias, the low cloud fraction bias is even larger (Figures 5g and 5k). The global mean bias of low cloud fraction is −0.194 and −0.197 in OLD and CTRL, respectively. As shown in Figure 5o, the most significant reduction of low cloud fraction in CTRL is in the high latitude land area. The low cloud fraction reduction is attributed to the change of temperature range for cloud water autoconversion as described in Appendix A. It allows cloud water autoconversion at a lower temperature. Due to the under-prediction of middle and low cloud fractions, the total cloud fraction is also under-predicted (Figures 5h and 5i). However, we can still see that the global mean bias and RMSE of total cloud fraction are reduced because of significant total cloud increment over the Southern Ocean (Figure 5p).

We further evaluate the liquid and ice water paths (compared with ERA5) and precipitation (compared with GPM) predictions. As shown in Figures 6a, 6d and 6g, SHiELD's predicted liquid water path is similar to ERA5 regarding its geographical distribution. However, both OLD and CTRL over-predict the liquid water path around the extra-tropical storm track area with a positive bias of 7.328 $g\ m^{-2}$ and 2.974 $g\ m^{-2}$ respectively (also see Figure S5 in Supporting Information S1). Compared with OLD, the bias and RMSE are both notably reduced in CTRL. As shown in Figure 6j, most of the significant reduction of liquid water path with the value of about 30 $g\ m^{-2}$ is at the middle to high latitudes, where the model over-predicts the liquid water path. This is consistent with the low cloud fraction change shown in Figure 5o, which is mainly due to the temperature range change for

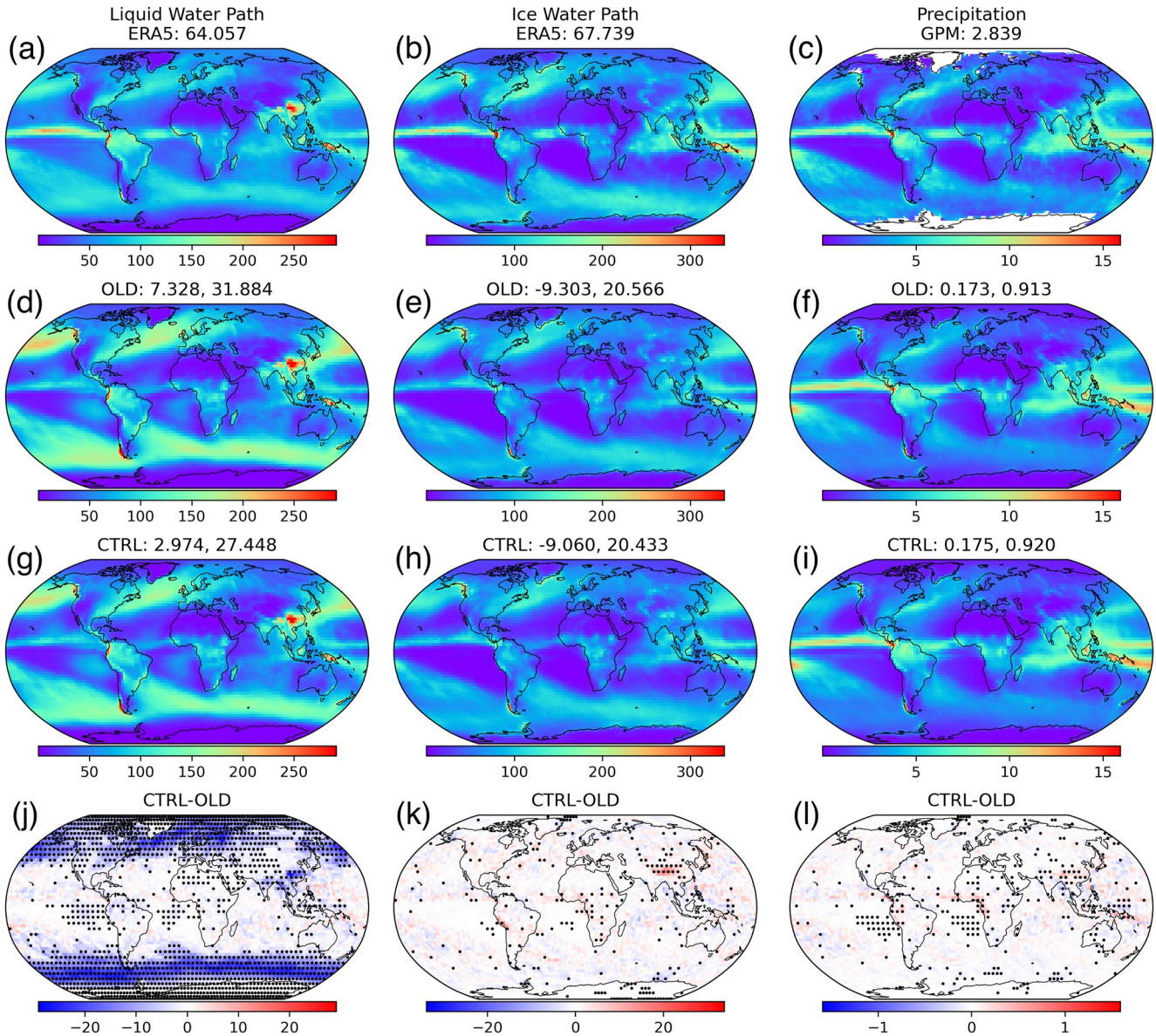

Figure 6. From left to right are the 10-day averaged liquid water path (LWP), ice water path (IWP), and precipitation rate (PRE) from (a–c) ERA5 or Global Precipitation Measurement (GPM), (d–f) OLD, (g–i) CTRL, and (j–l) CTRL minus OLD. The numbers in the title of (a–c) are the global mean of liquid water path or ice water path (unit: $g\ m^{-2}$) or precipitation (unit: $mm\ day^{-1}$), and (d–i) are the bias and root-mean-square error to ERA5 or GPM. The dotted area in (j–l) is the area with a 95% significant difference.

cloud water autoconversion. Compared with the ERA5, the geographical distributions of the ice water path are well-predicted in both OLD and CTRL (Figures 6b, 6e and 6h). The bias and RMSE of CTRL are only slightly smaller than those of OLD. Both values are about $-9\ g\ m^{-2}$. Not surprisingly, the difference between OLD and CTRL is insignificant, shown from the difference panel in Figure 6k. Regarding the precipitation forecasts (Figures 6f and 6i), both OLD and CTRL can well-predict the massive precipitation rates along the Intertropical Convergence Zone (ITCZ) area and in the extra-tropical storm track area. However, both OLD and CTRL predict slightly more precipitation (about 0.17 $mm\ day - 1$) globally. CTRL's precipitation prediction has a slightly larger bias and RMSE than OLD, but the differences are insignificant (Figure 6l).

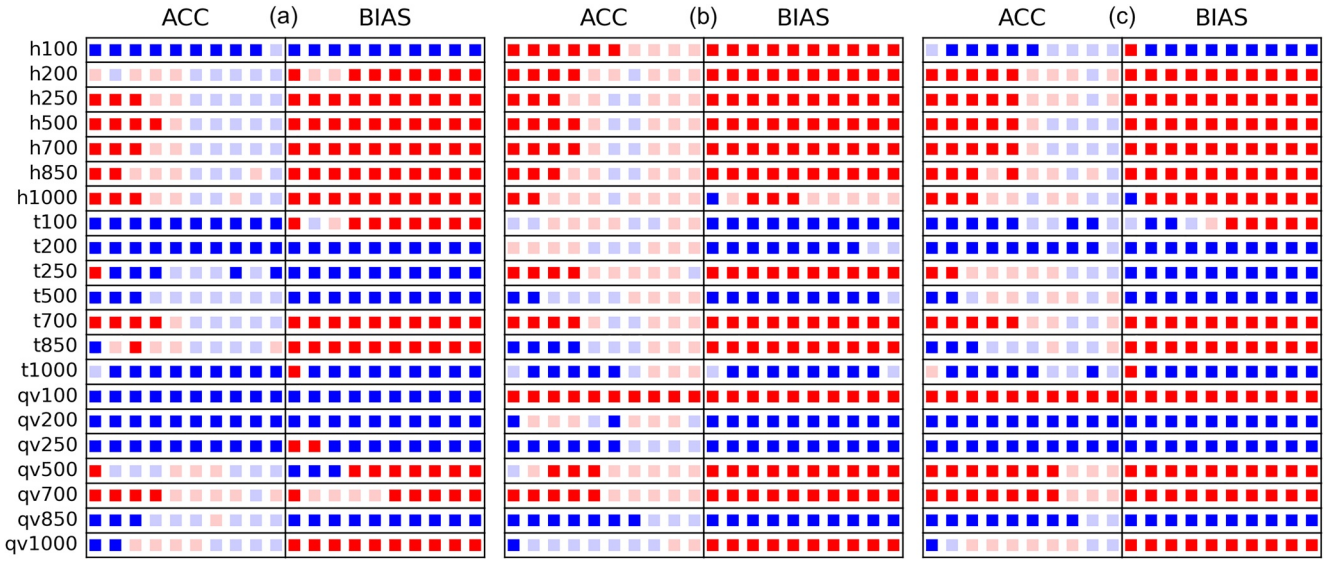

Figure 7. Similar to Figure 4, but for comparison between (a) CTRL and CPSD, (b) CTRL and AERO, (c) CTRL and CPSD_AERO.

6. Impacts of PSD and CDNC on Weather Prediction

In this section, three sensitivity experiments (CPSD, AERO, and CPSD_AERO) are used to evaluate the impacts of the PSD in the GFDL MP v3, as well as the use of time-and-space varying prescribed climatological aerosol in calculating CDNC, on weather prediction. The scorecards of the comparison between CTRL and each of the sensitivity experiments are shown in Figure 7. It can be found that the ACCs of geopotential height in CPSD are higher than those in CTRL in the first 5-day forecast. Meanwhile, compared to CTRL, the biases of geopotential height prediction are significantly smaller during the entire 10-day forecast (Figure 7a). On the other hand, the temperature and specific humidity predictions in the CPSD are generally improved at levels lower than 500 hPa but significantly degraded at 500 hPa and above. The differences in the temperature ACC between the CPSD and CTRL are hard to quantify in the time evolution plots, but their difference in temperature biases are evident (see Figure S4 in Supporting Information S1). Compared to CTRL, the predicted temperature in CPSD is lower at 200 and 250 hPa but higher at 500 hPa, and the predicted specific humidity in CPSD is lower at 100, 200, and 250 hPa.

To understand the reason for the temperature and specific humidity decreasing at the middle to upper Troposphere (except that temperature at 500 hPa increases) in CPSD than CTRL, we first examine the cloud fraction prediction (Figure 8). CPSD predicted a similar amount of high cloud fraction to CTRL (Figure 8e). The biases of the high cloud fraction prediction in CPSD and CTRL are very close. The RMSE of the high cloud fraction prediction in CPSD is slightly larger than that in CTRL during the entire 10-day forecast (Figure 8a). In contrast, there is a significant increment of the RMSE of middle cloud fraction prediction up to 0.01 on day 10 in CTRL when compared to CPSD (Figure 8b). Comparing the bias of middle cloud fraction prediction shown in Figure 8f, the predicted middle cloud fraction is around 0.02 larger in CPSD than that in CTRL. It implies that more water vapor is deposited into solid hydrometeor to the middle clouds in CPSD. The associated latent heat releases and then warms up the air in the middle Troposphere. Due to the decrease of the water vapor in the upper Troposphere, the longwave radiation absorption reduces. Meanwhile, the increasing middle cloud fraction further increases cloud top solar albedo enhancing the cloud top cooling in the above air. Therefore, the atmospheric temperature is lower in CPSD than in CTRL. These are consistent with what we found in the temperature and specific humidity prediction in Figure 7a.

The increases of the predicted cloud ice in CPSD are also shown by the ice water path (Figure 9e). The bias of ice water path prediction changes from -11 to 3 $g\ m^{-2}$ from CTRL to CPSD. The bias of the absolute ice water path prediction is much smaller in CPSD compared to that in CTRL. On the other hand, the RMSE of ice water path prediction is much larger in CPSD than that in CRTL (Figure 9b). The significantly larger predicted ice water path in CPSD is due to the increases in the cloud ice terminal fall velocity, which is from the redefinition

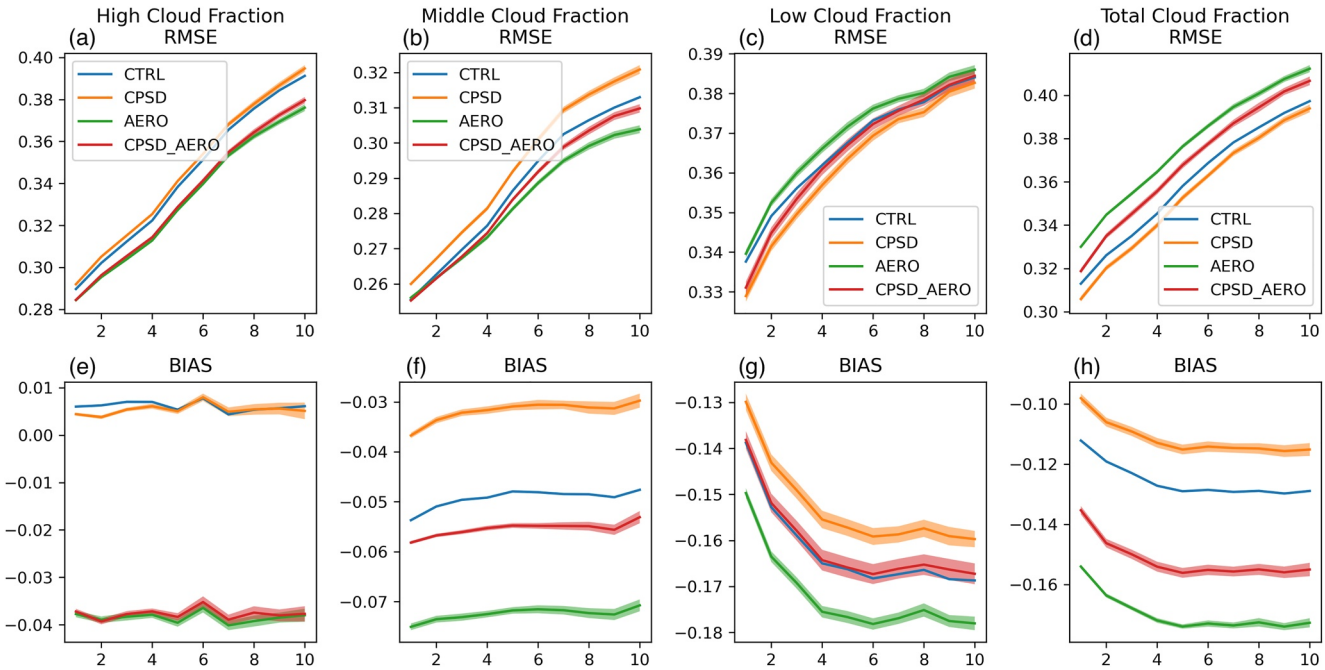

Figure 8. From left to right are the 10-day evolution of (a and e) high, (b and f) middle, (c and g) low, and (d and h) total cloud fractions of (blue) CTRL, (orange) CPSD, (green) AERO, and (red) CPSD_AERO. Top row is root mean square error (unit: 1); bottom row is bias (unit: 1). The shaded area is the area with a 95% significant difference to CTRL.

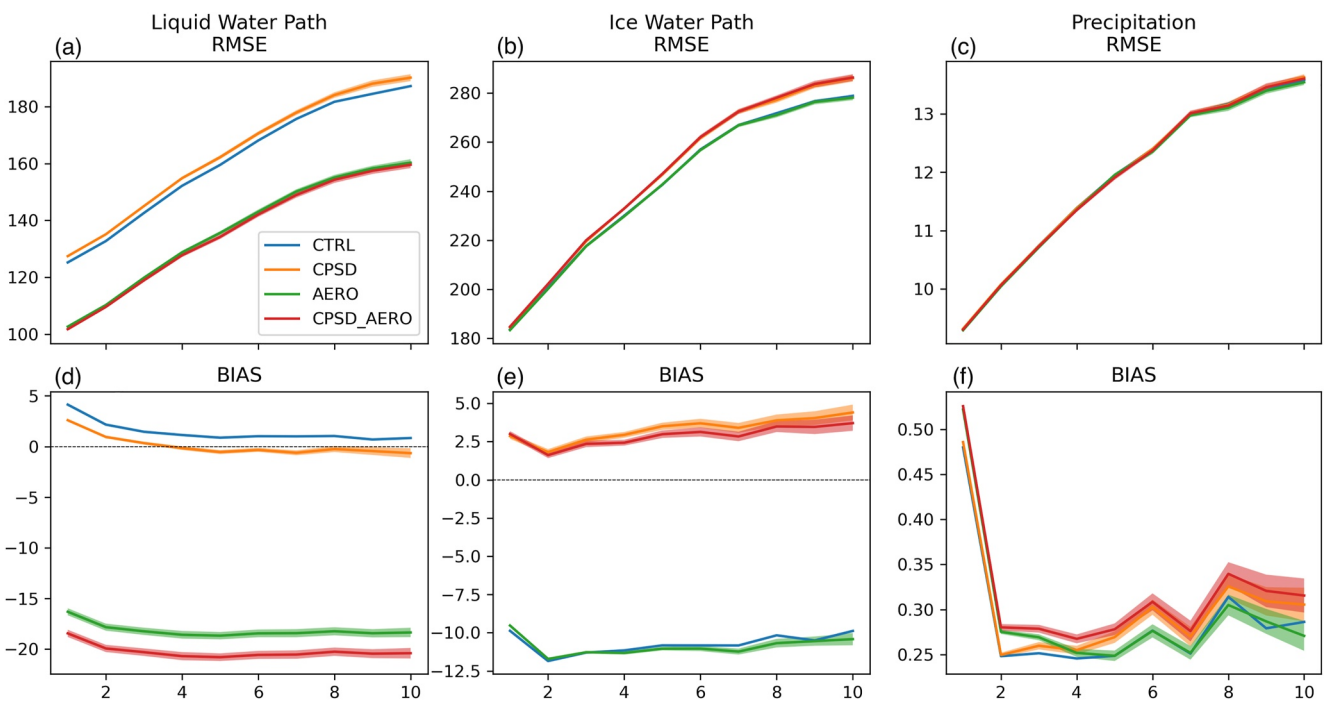

Figure 9. From left to right are the 10-day evolution of (a and d) liquid water path, (b and e) ice water path, and (c and f) precipitation of (blue) CTRL, (orange) CPSD, (green) AERO, and (red) CPSD_AERO. Top row is root mean square error (unit: $g\ m^{-2}$); bottom row is bias (unit: $g\ m^{-2}$). The shaded area is the area with a 95% significant difference to the CTRL.

of cloud ice PSD (Figure 2b). As a result, it brings more cloud ice sediment to lower levels, while the reduction of cloud ice at higher levels causes more deposition of water vapor. The improvement of low cloud fraction prediction (Figures 8c and 8g) possibly contributes to the improvement of the temperature and specific humidity prediction in the lower Troposphere (Figure 7a). The degradation of the precipitation prediction is small in CPSD (Figures 9c and 9f).

The upgrade of the CDNC calculation in AERO directly affects the autoconversion of cloud water to rainwater. Figure 7b shows that the prediction skill of geopotential height, temperature, and specific humidity are generally improved. Particularly, the ACCs of geopotential height substantially increase with significant bias reductions. Due to less produced CDNC in AERO than in CTRL, it is relatively easier for the cloud water to convert to rain and fall to the surface in AERO than in CTRL. Therefore, the low cloud fraction in AERO is reduced by about 0.01 (Figure 8g), and the liquid water path is also significantly reduced by nearly 20 $g\ m^{-2}$ (Figure 9d). The reduction of cloud fraction and the resultant reduced cloud albedo lead to a warmer surface. With a stronger surface heat exchange, the lower Troposphere is warmed up. Extra heat is transported from the lower Troposphere to the air above, inducing a warmer middle to upper Troposphere. It is relatively harder for the water vapor to condense or deposit in the warmer air. Therefore, the high and middle cloud fractions (Figures 8e and 8f) further decrease by 0.04 and 0.02, respectively. Even with more cloud water to rain autoconversion in AERO than in CTRL, the changes of precipitation prediction are still minor (Figures 9c and 9f), which may be related to some compensation from the increase of convective precipitation.

Another feature of using the MERRA2 aerosol to calculate CDNC is that it has a seasonal cycle Figure 3d and also Figure S1 in Supporting Information S1. We further evaluate the impact of the seasonal cycle of CDNC on weather prediction. Since CDNC is mainly used in warm cloud microphysics, the forecast of 500 hPa geopotential height and 700 hPa temperature are evaluated. Figure 10 shows some seasonal variation on 500 hPa geopotential height and 700 hPa temperature forecast. In the first 4-day forecast, AERO exhibits significantly smaller RMSE than CTRL. RMSE difference in summer is larger than all other seasons, which correlates to the least CDNC in summer shown in 3days. It indicates less CDNC in favor of weather forecasts in the lower Troposphere. After 4 day forecast, although the RMSE difference is much larger than that in the first 4 days, most of which are insignificant. The ninth-to tenth-day forecast of 500 hPa geopotential height and 700 hPa temperature in spring is the exception. AERO's forecast is significantly better than CTRL's forecast.

Finally, the impacts of combining the more realistic PSD and the climatological aerosol calculated CDNC are evaluated (Exp. of CPSD_AERO). Figure 7c shows that AERO can improve the degradation of the forecast skill shown in CPSD. For example, the forecasts of the geopotential height of CPSD_AERO during the first 5 days are significantly improved compared to CTRL. Moreover, temperature forecasts at 250 and 500 hPa, and forecasts of specific humidity at 100, 500, and 700 hPa are generally improved in CPSD_AERO. Generally speaking, there are more improved forecast fields than degraded ones in CPSD_AERO than in CTRL (Figure 7c). It is interesting to find in Figure 8 that the high cloud fraction prediction in CPSD_AERO is quite close to AERO, but the middle, low, and total cloud fraction prediction in CPSD_AERO is in between CPSD and AERO. Differently, the prediction of the liquid water path of CPSD_AERO is close to AERO, but the ice water path of CPSD_AERO is close to CPSD. Since the update of the PSD alters many microphysical processes, but the update of the CDNC changes the cloud water to rainwater autoconversion only, it is difficult to explain these interesting findings. We leave these to further research.

In all experiments, we find that the change of PSD in the cloud water and the cloud ice or the use of climatological aerosol for CDNC calculation only exerts a minor impact on the precipitation prediction (Figures 9c and 9f). It is possibly due to the change of large-scale precipitation being small compared to the change of cloud content. In addition, the change of the large-scale precipitation could be compensated by an increase in convective precipitation. Additionally, precipitation can be influenced by microphysical processes that do not involve the change of PSD and CDNC.

7. Summary and Discussion

This paper documents the third version of the Geophysical Fluid Dynamics Laboratory cloud microphysics scheme (GFDL MP v3) that is upgraded from the previous versions of the GFDL MP used in the Global Forecast System (GFS), the System for High-resolution prediction on Earth-to-Local Domains (SHiELD), and a broader

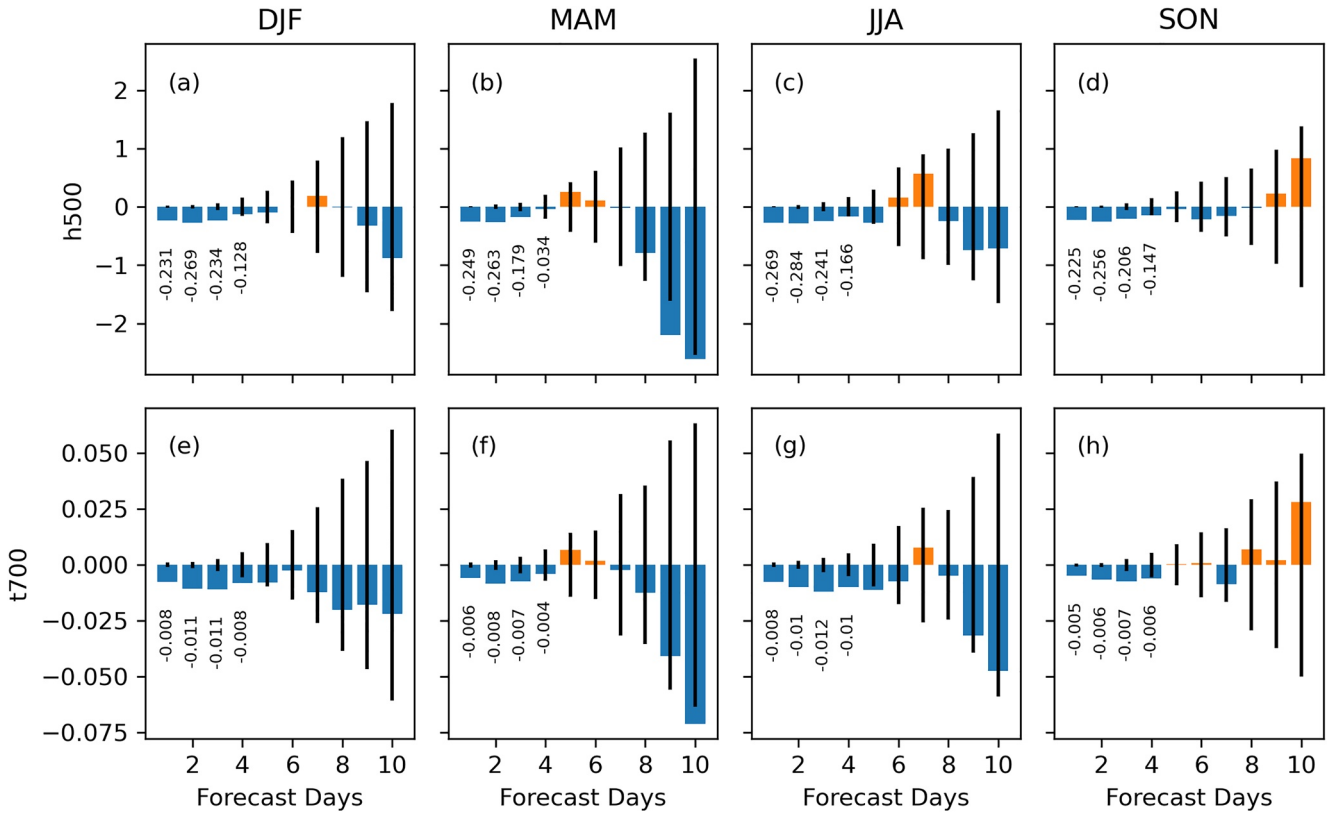

Figure 10. From left to right are the root-mean-square error (RMSE) difference of (a–d) 500 hPa geopotential height and (e–h) 700 hPa temperature forecasts between AERO and CTRL in (a,e) winter (DJF: December, January, February), (b and f) spring (MAM: March, April, May), (c and g) summer (JJA: June, July, August), and (d and h) fall (SON: September, October, November). Blue/orange bars are the RMSE difference; blue bars depict negative values while orange bars depict positive values; black lines indicate the 95% significance levels; numbers under the blue bars are the values of the RMSE difference in the first 4-day forecast. Negative RMSE difference means AERO is better than CTRL in the forecast, and vice verses. RMSE difference inside the 95% significance levels means the difference is insignificant, and vice verses.

community through the UFS. Compared with the GFDL MP v2, the GFDL MP v3 is featured with the following upgrades: (a) the code has been reorganized, optimized, and modularized into functions; (b) the particle size distribution (PSD) used in the scheme for all five hydrometeor categories are redefined as gamma or exponential distribution; (c) particle concentration, effective diameter, optical extinction, mass specific ratio, radar reflectivity factor, and terminal velocity are all redefined based on the new distributions; (d) accretion, evaporation, sublimation, deposition, melting, and freezing microphysical processes are all reformulated based on the new distributions; (e) constant cloud droplet number concentration (CDNC) is replaced with that calculated from climatological aerosols in the Modern-Era Retrospective analysis for Research and Applications, version 2 (MERRA2). The GFDL MP v3 ensures an overall microphysical consistency and easily permits the future introduction of new PSDs, microphysical processes, and multi-moment distributions.

The impacts of the GFDL MP upgrade item 1) on global weather, cloud, and precipitation predictions in SHiELD are comprehensively evaluated. The comparisons between the two sets of experiments show that GFDL MP v3 significantly improves the geopotential height prediction up to 7 days in term of anomaly correlation coefficient (ACC) and throughout 10-day forecast in term of bias, which indicates general improvement of the atmospheric circulation and heating in the Troposphere. The temperature prediction is generally better in GFDL MP v3 than in GFDL MP v2. The specific humidity prediction is better in GFDL MP v3 than GFDL MP v2 in the upper Troposphere but worse in the lower Troposphere. High, middle, and total cloud fractions predictions are improved in GFDL MP v3. Low cloud fraction prediction degrades in GFDL MP v3, but liquid water path prediction improves substantially. There is a minor change in the ice water path and precipitation prediction from GFDL MP v2 and GFDL MP v3. It is believed that the noticed degradation could be improved with further model development.

Furthermore, the impacts of the GFDL MP upgrade items 2 to 5 are evaluated using the base GFDL MP v3 as a reference. The use of more realistic PSD and climatological aerosol calculated CDNC significantly improves the geopotential height prediction compared with the original PSD and constant CDNC. Temperature and specific humidity predictions at the upper Troposphere significantly degrade with the PSD upgrade, but are mixed with improvement and degradation with the CDNC upgrade. Among all upgrades, the PSD upgrade shows the best prediction of low and total cloud fractions but the worst prediction of high and middle cloud fractions, while the CDNC upgrade shows the best prediction of high and middle cloud fractions but the worst prediction of low and total cloud fractions. The combination of the PSD and the CDNC upgrades is generally excellent in cloud fraction prediction. The combination of the PSD and the CDNC upgrades shows the best liquid water path prediction with the lowest RMSE, but with a very large negative bias. The PSD upgrade shows the largest RMSE of liquid water path prediction, although its bias is the smallest. In contrast, the combination of the PSD and the CDNC upgrades shows the smallest bias in ice water path prediction but a larger RMSE of the ice water path prediction. These results indicate that the global mean liquid and ice water paths are very different between the ERA5 and SHiELD. Note that we use ERA5 to evaluate liquid water path and ice water path prediction because this is the only reliable validation data set available for the entire forecast time period. More reliable direct observations will be used for this purpose in the future.

There are still some caveats for the GFDL MP v3. For example, the prediction of 500 hPa temperature tends to be worse (lower ACC and larger warm bias) than that in the GFDL MP v2. This bias has been identified in SHiELD for a long time. A possible reason is that the convective heating of the middle Troposphere is too strong, and radiative cooling is not enough to compensate. Further investigation is still needed to alleviate this bias. Middle, low, and total cloud fractions are under-predicted in SHiELD regardless of the version of the GFDL MP used. We plan to extend our cloud fraction diagnosis in the GFDL MP to include sub-grid terrain and static energy to better represent sub-grid variability, especially over complex terrain. We are also working on a more physically-motivated definition of parameters in the PSD (e.g., $\mu > 1$ for cloud ice and precipitation particles) using observations from flights and incorporating the effects of temperature, wind, and pressure on the PSD. This aims to create a more realistic relationship between meteorological fields and PSD from observational data, and to resolve the degradation of upper-tropospheric biases in temperature and humidity. All PSDs defined in the GFDL MP are currently based on the spherical geometry assumption. Some studies have shown a large difference in PSDs using non-spherical geometry assumption (Wu and McFarquhar (2016) and references therein). Future development will take this into account. We also plan to eliminate the low bias in low-to-middle latitudes and high bias in high latitudes, of liquid water path, and to improve the seamlessness of the GFDL MP across space and time scales, as appropriate for the wide range of applications of SHiELD, GFS, and Unified Forecast System (UFS) from convective-scale to seasonal prediction. We also will consider a double-moment extension of the GFDL MP if it improves the model's prediction skill, which includes the cloud water activation using actual aerosol mass, cloud ice nucleation.

Appendix A: The GFDL Cloud Microphysics Version 3

The third version of the GFDL MP follows version 1 (Zhou et al., 2019) and version 2 (Harris, Zhou, et al., 2020). This new version of the GFDL MP features three major upgrades: (a) the code is entirely reorganized, optimized, and modularized into functions, (b) there are various scientific modifications to the microphysical processes, and (c) several optional definitions and microphysical processes are added. The scientific modifications used for this paper include:

1. Redefined supersaturation in the ice processes to use the same saturation tables as other microphysical processes, ensuring consistency;
2. Allow cloud water autoconversion in the larger temperature range ($>-40°C$) liquid water exists;
3. Split rain evaporation and accretion more physically and consistently;
4. Remove redundant cloud ice melting before falling;
5. Remove several unnecessary temperature limits and ensure positive hydrometeor specific ratios;
6. Remove time step splitting between fast saturation adjustment and full microphysics;
7. Combine snow and graupel for snow effective radius diagnosis, to include the radiative effect of graupel.

There are also many options added to the GFDL MP not used in this paper but that can be used in other applications of SHiELD (T-SHiELD, C-SHiELD, and S-SHiELD), toward unified modeling in which there is a single modeling system with one code, one executable, and one workflow (Harris, Zhou, et al., 2020). Those new options include:

1. New cloud fraction diagnostic schemes;
2. New cloud ice nucleation schemes;
3. New cloud ice generation schemes;
4. New cloud ice fall velocity diagnostic schemes;
5. New cloud water and cloud ice diagnostic effective radii schemes;
6. New radar reflectivity diagnostics;
7. Wegener-Bergeron-Findeisen process;

Appendix B: Quantities Characterizing Cloud Parameters

The particle concentration (N, unit: m^{-3}), effective diameter (D_{eff}, unit: m), optical extinction (β, unit: m^{-1}), mass specific ratio (q, unit: $kg\ kg^{-1}$), radar reflectivity factor (Z, unit: m^3), and terminal velocity (V, unit: $m\ s^{-1}$) can be calculated by integrating the (particle size distribution) PSD over all diameters:

$$N = \int_0^\infty n(D)\,dD = \frac{n_0\Gamma(\mu)}{\lambda^\mu}, \tag{B1}$$

$$D_{\text{eff}} = \frac{\int_0^\infty D^3 n(D)\,dD}{\int_0^\infty D^2 n(D)\,dD} = \frac{\mu+2}{\lambda}, \tag{B2}$$

$$\beta = \frac{\pi}{2}\int_0^\infty D^2 n(D)\,dD = \frac{\pi n_0\Gamma(\mu+2)}{2\lambda^{\mu+2}}, \tag{B3}$$

$$q = \frac{\pi}{6}\frac{\rho'}{\rho}\int_0^\infty D^3 n(D)\,dD = \frac{\pi\rho' n_0\Gamma(\mu+3)}{6\rho\lambda^{\mu+3}}, \tag{B4}$$

$$Z = \int_0^\infty D^6 n(D)\,dD = \frac{n_0\Gamma(\mu+6)}{\lambda^{\mu+6}}, \tag{B5}$$

$$V = \frac{\int_0^\infty vD^3 n(D)\,dD}{\int_0^\infty D^3 n(D)\,dD} = \frac{\alpha\Gamma(\mu+\beta+3)}{\lambda^\beta\Gamma(\mu+3)}. \tag{B6}$$

Where $v = \alpha D^\beta$ is approximately written as power-law relation following Straka (2009). The density (ρ'), leading coefficient α, and the power β of each hydrometeor category are listed in Table 1. ρ is the density of air. In the single-moment case where the mass specific ratio (q) is a prognostic variable, the slope parameter (λ) can be derived from Equation B4:

$$\lambda = \left[\frac{\pi\rho' n_0\Gamma(\mu+3)}{6\rho q}\right]^{1/(\mu+3)}. \tag{B7}$$

Appendix C: Microphysical Processes

Accretion between each two falling hydrometeor categories follows Wisner et al. (1972). The accretion rate between cloud x and y (P_{xacy}, accretion of y by x, unit: $kg\ kg^{-1}\ s^{-1}$) is reformulated after putting the gamma distribution in and integrating the particle size from zero to infinity:

$$\begin{aligned} P_{xacy} &= \int_0^\infty\int_0^\infty \frac{\pi^2}{24}E_{xy}\left|V_x - V_y\right|\frac{\rho_{y0}}{\rho}(D_x+D_y)^2 D_y^3 n_x(D_x)\,n_y(D_y)\,dD_x dD_y \\ &= \frac{\pi^2}{24}E_{xy}n_{x0}n_{y0}\left|V_x - V_y\right|\frac{\rho_{y0}}{\rho}\left[\frac{\Gamma(\mu_x)\Gamma(\mu_y+5)}{\lambda_x^{\mu_x}\lambda_y^{\mu_y+5}} + \frac{\Gamma(\mu_x+2)\Gamma(\mu_y+3)}{\lambda_x^{\mu_x+2}\lambda_y^{\mu_y+3}} + \frac{2\Gamma(\mu_x+1)\Gamma(\mu_y+4)}{\lambda_x^{\mu_x+1}\lambda_y^{\mu_y+4}}\right], \end{aligned} \tag{C1}$$

where V_x and V_y are the terminal velocities of cloud x and y, respectively. E_{xy} is the collection efficiency between cloud x and y. Specifically, $E_{rw} = 0.35$, $E_{ri} = 1.0$, $E_{sw} = 1.0$, $E_{si} = 0.35$, $E_{sr} = 1.0$, $E_{gw}/E_{hw} = 1 \times 10^{-4}$, $E_{gi}/E_{hi} = 0.05$, $E_{gr}/E_{hr} = 1.0$, and $E_{gs}/E_{hs} = 0.01$. This formula can be simplified when one of the two hydrometeor categories (e.g., y) does not fall and is distributed mono-dispersedly as:

$$P_{xacy} = \int_0^\infty \frac{\pi}{4} E_{xy} q_y V_x D_x^2 n_x (D_x)\, dD_x = \frac{\pi E_{xy} n_{x0} \alpha_x q_y \Gamma(\mu_x + \beta_x + 2)}{4\lambda^{\mu_x+\beta_x+2}}, \tag{C2}$$

The exponential case ($\mu = 1$) of Equations C1 and C2 are widely used in the Y. Lin et al. (1983) scheme and in early versions of the GFDL MP scheme. Some studies (Mizuno, 1990; Murakami, 1990) have pointed out that V_x and V_y are simplified as mean terminal velocities. If cloud x and y have a broad velocity spectra, accretion rate P_{xacy} is non-zero when $V_x = V_y$. The formula proposed in Mizuno (1990); Murakami (1990) will be implemented to the GFDL MP in the near future.

Evaporation, sublimation and deposition follow Byers (1965). The evaporation/sublimation/deposition rate (P_{ESD}, unit: $kg\ kg^{-1}\ s^{-1}$) is reformulated after putting the gamma distribution in and integrating the particle size from zero to infinity:

$$P_{ESD} = \int_0^\infty \frac{2\pi (S-1)}{\rho (A+B)} V_f Dn(D)\, dD = \frac{2\pi (S-1)}{\rho (A+B)} \frac{n_0 \Gamma(\mu+1)}{\lambda^{\mu+1}} V_f, \tag{C3}$$

where S is the ratio between saturated mixing ratio of water vapor (q_{sat}) and water vapor mixing ratio (q_v), A and B are thermodynamics terms defined as:

$$A = \frac{L^2}{K_a R_v T^2}, \tag{C4}$$

$$B = \frac{1}{\rho q_{sat} \psi}, \tag{C5}$$

where L is the latent heat coefficient, $K_a = 2.36 \times 10^{-2}\ J\ m^{-1}\ s^{-1}\ K^{-1}$ is the thermal conductivity of air, R_v is gas constant of water vapor, T is air temperature, and $\psi = 2.11 \times 10^{-5}\ m^2\ s^{-1}$ is diffusivity of water vapor.

The ventilation coefficient (V_f) in Equation C3 is defined followed Beard and Pruppacher (1971). After putting the gamma distribution in and integrating the particle size from zero to infinity, V_f is reformatted as:

$$V_f = 0.78 + 0.31 S_c^{1/3} \nu^{1/2} \frac{\int_0^\infty V^{1/2} D^{3/2} n(D)\, dD}{\int_0^\infty Dn(D)\, dD} = 0.78 + 0.31 S_c^{1/3} \nu^{-1/2} \frac{\alpha^{1/2} \Gamma\left(\mu + \frac{\beta+3}{2}\right)}{\lambda^{\mu+\frac{\beta+3}{2}}} \frac{\lambda^{\mu+1}}{\Gamma(\mu+1)}, \tag{C6}$$

where $\nu = 1.259 \times 10^{-5}\ m^2\ s^{-1}$ is the kinematic viscosity of air and $S_c = \nu/\psi$ is the Schmidt number.

The melting process follows Mason (1971). The melting rate (P_{melt}, unit: $kg\ kg^{-1}\ s^{-1}$) is reformulated after putting the gamma distribution in and integrating the particle size from zero to infinity:

$$\begin{aligned} P_{melt} &= \int_0^\infty \frac{2\pi}{\rho L} \left[K_a (T - T_0) - L\psi\rho (q_{sat} - q_v)\right] V_f Dn(D)\, dD \\ &= \frac{2\pi}{\rho L} \left[K_a (T - T_0) - L\psi\rho (q_{sat} - q_v)\right] \frac{n_0 \Gamma(\mu+1)}{\lambda^{\mu+1}} V_f, \end{aligned} \tag{C7}$$

where T_0 is the freezing temperature.

At last, the rain freezing process follows Wisner et al. (1972). The freezing rate (P_{fr}, unit: $kg\ kg^{-1}\ s^{-1}$) is reformulated after putting the gamma distribution in and integrating the particle size from zero to infinity:

$$\begin{aligned} P_{fr} &= \int_0^\infty \frac{\pi^2}{36} D^6 \frac{\rho'}{\rho} B' \exp\left[A'(T_0 - T) - 1\right] n(D)\, dD \\ &= \frac{\pi^2}{36} n_0 \frac{\rho'}{\rho} B' \exp\left[A'(T_0 - T) - 1\right] \frac{\Gamma(\mu+6)}{\lambda^{\mu+6}}, \end{aligned} \tag{C8}$$

where $A' = 0.66\ K^{-1}$ and $B' = 100\ m^{-3}\ s^{-1}$ are two constant parameters following Bigg (1953).

The following microphysical processes remain the same from GFDL MP v2: (a) condensation and evaporation of cloud water, (b) deposition and sublimation of cloud ice, (c) cloud ice freezing and melting, (c) cloud water autoconversion, (e) cloud ice aggregation or autoconversion, (f) snow aggregation or autoconversion. Future GFDL MP development will include the particle size distribution to these remaining processes.

Data Availability Statement

The source codes of SHiELD are available at https://doi.org/10.5281/zenodo.5800223. The corresponding data is available at https://doi.org/10.5281/zenodo.5800259. The COSP2 software package can be accessed from https://github.com/CFMIP/COSPv2.0. The MERRA2 data can be obtained from https://goldsmr5.gesdisc.eosdis.nasa.gov/data. The ERA5 data can be obtained from https://cds.climate.copernicus.eu/#!/search?text=ERA5&type=dataset. The CALIPSO-GOCCP data can be obtained from https://climserv.ipsl.polytechnique.fr/cfmip-obs/Calipso_goccp.html. The GPM data can be obtained from https://disc.gsfc.nasa.gov/datasets/GPM_3IMERGHH_06/summary?keywords=gpm%20imerg.

Acknowledgments
The authors want to thank Dr. Shian-Jiann Lin, who developed the early version of the GFDL MP more than 10 years ago. His great ideas and philosophy are still in the latest version of this scheme. The authors also thank Dr. Xi Chen for his comments and suggestions on the aerosol implementation. Many thanks also go to the GFDL FV3 team, who support the development of the GFDL MP in many ways. The authors also want to thank Dr. Songmiao Fan, Dr. Zhihong Tan, Dr. Nadir Jeevanjee, and three anonymous reviewers for their valuable comments and suggestions to improve the quality of this manuscript. Zhou and Gao are supported under awards NA18OAR4320123, NA19OAR0220146, and NA19OAR0220147 from the National Oceanic and Atmospheric Administration (NOAA), U.S. Department of Commerce.

References

Arnold, N., Putman, W., & Freitas, S. (2020). Impact of resolution and parameterized convection on the diurnal cycle of precipitation in a global nonhydrostatic model. *Journal of the Meteorological Society of Japan*, *98*, 1279–1304. https://doi.org/10.2151/jmsj.2020-066

Baldauf, M., Seifert, A., Forstner, J., Majewski, D., Raschendorfer, M., & Reinhardt, T. (2011). Operational convective-scale numerical weather prediction with the Cosmo model: Description and sensitivities. *Monthly Weather Review*, *139*, 3887–3905. https://doi.org/10.1175/Mwr-D-10-05013.1

Bauer, P., Thorpe, A., & Brunet, G. (2015). The quiet revolution of numerical weather prediction. *Nature*, *525*, 47–55. https://doi.org/10.1038/nature14956

Beard, K., & Pruppacher, H. (1971). A wind tunnel investigation of the rate of evaporation of small water drops falling at terminal velocity in air. *Journal of the Atmospheric Sciences*, *28*, 1455–1464. https://doi.org/10.1175/1520-0469(1971)028<1455:awtiot>2.0.co;2

Bigg, E. (1953). The supercooling of water. *Proceedings of the Physical Society*, *66*, 688–694. https://doi.org/10.1088/0370-1301/66/8/309

Bodas-Salcedo, A., Webb, M., Bony, S., Chepfer, H., Dufresne, J., Klein, S., et al. (2011). Cosp satellite simulation software for model assessment. *Bulletin of the American Meteorological Society*, *92*, 1023–1043. https://doi.org/10.1175/2011bams2856.1

Boucher, O., & Lohmann, U. (1995). The sulfate-CCN-cloud albedo effect—A sensitivity study with 2 general-circulation models. *Tellus Series B Chemical and Physical Meteorology*, *47*, 281–300. https://doi.org/10.1034/j.1600-0889.47.issue3.1.x

Byers, H. (1965). *Elements of cloud physics*. The University of Chicago Press.

Chen, J., & Lin, S. (2011). The remarkable predictability of inter-annual variability of Atlantic hurricanes during the past decade. *Geophysical Research Letters*, *38*, L11804. https://doi.org/10.1029/2011gl047629

Chen, J., & Lin, S. (2013). Seasonal predictions of tropical cyclones using a 25-km-resolution general circulation model. *Journal of Climate*, *26*, 380–398. https://doi.org/10.1175/Jcli-D-12-00061.1

Chen, J., Lin, S., Magnusson, L., Bender, M., Chen, X., Zhou, L., et al. (2019). Advancements in hurricane prediction with NOAA's next-generation forecast system. *Geophysical Research Letters*, *46*, 4495–4501. https://doi.org/10.1029/2019gl082410

Chen, J., Lin, S., Zhou, L., Chen, X., Rees, S., Bender, M., & Morin, M. (2019). Evaluation of tropical cyclone forecasts in the next generation global prediction system. *Monthly Weather Review*, *147*, 3409–3428. https://doi.org/10.1175/Mwr-D-18-0227.1

Chepfer, H., Bony, S., Winker, D., Cesana, G., Dufresne, J., Minnis, P., et al. (2010). The GCM-oriented calipso cloud product (CALIPSO-GOCCP). *Journal of Geophysical Research*, *115*, D00H16. https://doi.org/10.1029/2009jd012251

Dong, J., Liu, B., Zhang, Z., Wang, W., Mehra, A., Hazelton, A., et al. (2020). The evaluation of real-time hurricane analysis and forecast system (HAFS) stand-alone regional (SAR) model performance for the 2019 Atlantic hurricane season. *Atmosphere*, *11*, 617. https://doi.org/10.3390/atmos11060617

Ek, M., Mitchell, K., Lin, Y., Rogers, E., Grunmann, P., Koren, V., et al. (2003). Implementation of Noah land surface model advances in the national centers for environmental prediction operational mesoscale eta model. *Journal of Geophysical Research*, *108*, 8851. https://doi.org/10.1029/2002jd003296

Fan, J., Wang, Y., Rosenfeld, D., & Liu, X. (2016). Review of aerosol-cloud interactions: Mechanisms, significance, and challenges. *Journal of the Atmospheric Sciences*, *73*, 4221–4252. https://doi.org/10.1175/Jas-D-16-0037.1

Federer, B., & Waldvogel, A. (1975). Hail and raindrop size distributions from a Swiss multicell storm. *Journal of Applied Meteorology*, *14*, 91–97. https://doi.org/10.1175/1520-0450(1975)014<0091:harsdf>2.0.co;2

Forbes, R., & Tompkins, A. (2011). An improved representation of cloud and precipitation (Technical Report). https://doi.org/10.21957/nfgulzhe

Forbes, R., Tompkins, A., & Untch, A. (2011). A new prognostic bulk microphysics scheme for the IFS (Technical Report). https://doi.org/10.21957/bf6vjvxk

Fu, Q. (1996). An accurate parameterization of the solar radiative properties of cirrus clouds for climate models. *Journal of Climate*, *9*, 2058–2082. https://doi.org/10.1175/1520-0442(1996)009<2058:aapots>2.0.co;2

Gao, K., Chen, J., Harris, L., Lin, S., Xiang, B., & Zhao, M. (2017). Impact of intraseasonal oscillations on the tropical cyclone activity over the Gulf of Mexico and Western Caribbean Sea in GFDL HIRAM. *Journal of Geophysical Research: Atmospheres*, *122*, 13125–13137. https://doi.org/10.1002/2017jd027756

Gao, K., Harris, L., Chen, J., Lin, S., & Hazelton, A. (2019). Improving AGCM hurricane structure with two-way nesting. *Journal of Advances in Modeling Earth Systems*, *11*, 278–292. https://doi.org/10.1029/2018ms001359

Gelaro, R., McCarty, W., Suarez, M., Todling, R., Molod, A., Takacs, L., et al. (2017). The modern-era retrospective analysis for research and applications, version 2 (MERRA-2). *Journal of Climate*, *30*, 5419–5454. https://doi.org/10.1175/JCLI-D-16-0758.1

Gunn, K., & Marshall, J. (1958). The distribution with size of aggregate snowflakes. *Journal of Meteorology*, *15*, 452–461. https://doi.org/10.1175/1520-0469(1958)015<0452:tdwsoa>2.0.co;2

Guo, H., Ming, Y., Fan, S., Zhou, L., Harris, L., & Zhao, M. (2021). Two-moment bulk cloud microphysics with prognostic precipitation in GFDL's atmosphere model AM4.0: Configuration and performance. *Journal of Advances in Modeling Earth Systems*, *13*, e2020MS002453. https://doi.org/10.1029/2020ms002453

Han, J., & Bretherton, C. (2019). Tke-based moist eddy-diffusivity mass-flux (EDMF) parameterization for vertical turbulent mixing. *Weather and Forecasting*, *34*, 869–886. https://doi.org/10.1175/Waf-D-18-0146.1

Han, J., Wang, W., Kwon, Y., Hong, S., Tallapragada, V., & Yang, F. (2017). Updates in the NCEP GFS cumulus convection schemes with scale and aerosol awareness. *Weather and Forecasting*, *32*, 2005–2017. https://doi.org/10.1175/Waf-D-17-0046.1

Harris, L., Chen, X., Zhou, L., & Chen, J. (2020). The nonhydrostatic solver of the GFDL finite-volume cubed-sphere dynamical core (Technical Report). https://doi.org/10.25923/9wdt-4895

Harris, L., & Lin, S. (2013). A two-way nested global-regional dynamical core on the cubed-sphere grid. *Monthly Weather Review*, *141*, 283–306. https://doi.org/10.1175/Mwr-D-11-00201.1

Harris, L., Lin, S., & Tu, C. (2016). High-resolution climate simulations using GFDL HIRAM with a stretched global grid. *Journal of Climate*, *29*, 4293–4314. https://doi.org/10.1175/Jcli-D-15-0389.1

Harris, L., Rees, S., Morin, M., Zhou, L., & Stern, W. (2019). Explicit prediction of continental convection in a skillful variable-resolution global model. *Journal of Advances in Modeling Earth Systems*, *11*, 1847–1869. https://doi.org/10.1029/2018ms001542

Harris, L., Zhou, L., Chen, X., & Chen, J. (2020). The gfdl finite-volume cubed-sphere dynamical core: Release 201912 (Technical Report). https://doi.org/10.25923/7h88-c534

Harris, L., Zhou, L., Lin, S., Chen, J., Chen, X., Gao, K., et al. (2020). Gfdl shield: A unified system for weather-to-seasonal prediction. *Journal of Advances in Modeling Earth Systems*, *12*, e2020MS002223. https://doi.org/10.1029/2020ms002223

Hazelton, A., Alaka, G., Cowan, L., Fischer, M., & Gopalakrishnan, S. (2021). Understanding the processes causing the early intensification of hurricane Dorian through an ensemble of the hurricane analysis and forecast system (HAFS). *Atmosphere*, *12*, 93. https://doi.org/10.3390/atmos12010093

Hazelton, A., Harris, L., & Lin, S. (2018). Evaluation of tropical cyclone structure forecasts in a high-resolution version of the multiscale GFDL FVGFS model. *Weather and Forecasting*, *33*, 419–442. https://doi.org/10.1175/Waf-D-17-0140.1

He, B., Bao, Q., Wang, X., Zhou, L., Wu, X., Liu, Y., et al. (2019). CAS FGOALS-F3-l model datasets for CMIP6 historical atmospheric model intercomparison project simulation. *Advances in Atmospheric Sciences*, *36*, 771–778. https://doi.org/10.1007/s00376-019-9027-8

Hersbach, H., Bell, B., Berrisford, P., Hirahara, S., Horanyi, A., Munoz-Sabater, J., et al. (2020). The ERA5 global reanalysis. *Quarterly Journal of the Royal Meteorological Society*, *146*, 1999–2049. https://doi.org/10.1002/qj.3803

Hoke, J., Phillips, G. N., DimegoTuccillo, J., & Sela, J. (1989). The regional analysis and forecast system of the national meteorological center. *Weather and Forecasting*, *4*, 323–334. https://doi.org/10.1175/1520-0434(1989)004<0323:traafs>2.0.co;2

Hong, Y., Hsu, K., Sorooshian, S., & Gao, X. (2004). Precipitation estimation from remotely sensed imagery using an artificial neural network cloud classification system. *Journal of Applied Meteorology*, *43*, 1834–1853. https://doi.org/10.1175/JAM2173.1

Houze, R. (2014). *Cloud dynamics* (Second edn). Academic Press.

Houze, R., Hobbs, P., Herzegh, P., & Parsons, D. (1979). Size distributions of precipitation particles in frontal clouds. *Journal of the Atmospheric Sciences*, *36*, 156–162. https://doi.org/10.1175/1520-0469(1979)036<0156:sdoppi>2.0.co;2

Huang, B., Wang, X., Kleist, D., & Lei, T. (2021). A simultaneous multiscale data assimilation using scale-dependent localization in GSI-based hybrid 4denvar for NCEP FV3-based gfs. *Monthly Weather Review*, *149*, 479–501. https://doi.org/10.1175/mwr-d-20-0166.1

Ikawa, M., & Saito, K. (1991). Description of a nonhydrostatic model developed at the forecast research department of the mri (Techical Report). https://doi.org/10.11483/mritechrepo.28

Jakob, C., & Klein, S. (2000). A parametrization of the effects of cloud and precipitation overlap for use in general-circulation models. *Quarterly Journal of the Royal Meteorological Society*, *126*, 2525–2544. https://doi.org/10.1002/qj.49712656809

Jeevanjee, N. (2017). Vertical velocity in the gray zone. *Journal of Advances in Modeling Earth Systems*, *9*, 2304–2316. https://doi.org/10.1002/2017ms001059

Khain, A., Beheng, K., Heymsfield, A., Korolev, A., Krichak, S., Levin, Z., et al. (2015). Representation of microphysical processes in cloud-resolving models: Spectral (bin) microphysics versus bulk parameterization. *Reviews of Geophysics*, *53*, 247–322. https://doi.org/10.1002/2014rg000468

Kogan, Y. (2013). A cumulus cloud microphysics parameterization for cloud-resolving models. *Journal of the Atmospheric Sciences*, *70*, 1423–1436. https://doi.org/10.1175/Jas-D-12-0183.1

Lamb, D., & Verlinde, J. (2011). *Physics and chemistry of clouds*. Cambridge University Press.

Li, J., Bao, Q., Liu, Y., Wu, G., Wang, L., He, B., et al. (2019). Evaluation of famil2 in simulating the climatology and seasonal-to-interannual variability of tropical cyclone characteristics. *Journal of Advances in Modeling Earth Systems*, *11*, 1117–1136. https://doi.org/10.1029/2018ms001506

Lin, S. (2004). A "vertically Lagrangian" finite-volume dynamical core for global models. *Monthly Weather Review*, *132*, 2293–2307. https://doi.org/10.1175/1520-0493(2004)132<2293:avlfdc>2.0.co;2

Lin, Y., Farley, R., & Orville, H. (1983). Bulk parameterization of the snow field in a cloud model. *Journal of Climate and Applied Meteorology*, *22*, 1065–1092. https://doi.org/10.1175/1520-0450(1983)022<1065:bpotsf>2.0.co;2

Liu, J., & Orville, H. (1969). Numerical modeling of precipitation and cloud shadow effects on mountain-induced cumuli. *Journal of the Atmospheric Sciences*, *26*, 1283–1298. https://doi.org/10.1175/1520-0469(1969)026<1283:nmopac>2.0.co;2

Manton, M., & Cotton, W. (1977). *Formulation of approximate equations for modeling moist deep convection on the mesoscale*. Doctoral dissertation, Colorado State University. Retrieved from https://mountainscholar.org/handle/10217/19926

Marshall, J., & Palmer, W. (1948). The distribution of raindrops with size. *Journal of Meteorology*, *5*, 165–166. https://doi.org/10.1175/1520-0469(1948)005<0165:tdorws>2.0.co;2

Martin, G., Johnson, D., & Spice, A. (1994). The measurement and parameterization of effective radius of droplets in warm stratocumulus clouds. *Journal of the Atmospheric Sciences*, *51*, 1823–1842. https://doi.org/10.1175/1520-0469(1994)051<1823:tmapoe>2.0.co;2

Mason, B. (1971). *The physics of clouds*, Clarendon Press.

McFarquhar, G., Hsieh, T., Freer, M., Mascio, J., & Jewett, B. (2015). The characterization of ice hydrometeor gamma size distributions as volumes in n0–lambda–mu phase space: Implications for microphysical process modeling. *Journal of the Atmospheric Sciences*, *72*, 892–909. https://doi.org/10.1175/jas-d-14-0011.1

Mizuno, H. (1990). Parameterization of the accretion process between different precipitation elements. *Journal of the Meteorological Society of Japan*, *68*, 395–398. https://doi.org/10.2151/jmsj1965.68.3_395

Morrison, H., & Gettelman, A. (2008). A new two-moment bulk stratiform cloud microphysics scheme in the community atmosphere model, version 3 (cam3). part i: Description and numerical tests. *Journal of Climate*, *21*, 3642–3659. https://doi.org/10.1175/2008jcli2105.1

Morrison, H., & Grabowski, W. (2008). A novel approach for representing ice microphysics in models: Description and tests using a kinematic framework. *Journal of the Atmospheric Sciences*, *65*, 1528–1548. https://doi.org/10.1175/2007jas2491.1

Murakami, M. (1990). Numerical modeling of dynamical and microphysical evolution of an isolated convective cloud. *Journal of the Meteorological Society of Japan*, *68*, 107–128. https://doi.org/10.2151/jmsj1965.68.2_107

Nogherotto, R., Tompkins, A., Giuliani, G., Coppola, E., & Giorgi, F. (2016). Numerical framework and performance of the new multiple-phase cloud microphysics scheme in REGCM4.5: Precipitation, cloud microphysics, and cloud radiative effects. *Geoscientific Model Development*, *9*, 2533–2547. https://doi.org/10.5194/gmd-9-2533-2016

Patel, R., Yuter, S., Miller, M., Rhodes, S., Bain, L., & Peele, T. (2021). The diurnal cycle of winter season temperature errors in the operational global forecast system (GFS). *Geophysical Research Letters*, *48*, e2021GL095101. https://doi.org/10.1029/2021gl095101

Pauluis, O., & Garner, S. (2006). Sensitivity of radiative–convective equilibrium simulations to horizontal resolution. *Journal of the Atmospheric Sciences*, *63*, 1910–1923. https://doi.org/10.1175/jas3705.1

Pollard, R., Rhines, P., & Thompson, R. (1973). The deepening of the wind-mixed layer. *Geophysical Fluid Dynamics*, *3*, 381–404. https://doi.org/10.1080/03091927208236105

Pruppacher, H., & Klett, J. (2010). *Microphysics of clouds and precipitation (Second revised and expanded edition with an introduction to cloud chemistry and cloud electricity ed*, Springer Dordrecht. https://doi.org/10.1007/978-0-306-48100-0

Putman, W., & Lin, S. (2007). Finite-volume transport on various cubed-sphere grids. *Journal of Computational Physics*, *227*, 55–78. https://doi.org/10.1016/j.jcp.2007.07.022

Randles, C., Da Silva, A., Buchard, V., Colarco, P., Darmenov, A., Govindaraju, R., et al. (2017). The merra-2 aerosol reanalysis, 1980—Onward, part I: System description and data assimilation evaluation. *Journal of Climate*, *30*, 6823–6850. https://doi.org/10.1175/JCLI-D-16-0609.1

Rasch, P., & Kristjánsson, J. (1998). A comparison of the CCM3 model climate using diagnosed and predicted condensate parameterizations. *Journal of Climate*, *11*, 1587–1614. https://doi.org/10.1175/1520-0442(1998)011<1587:acotcm>2.0.co;2

Rienecker, M., Suarez, M., Gelaro, R., Todling, R., Bacmeister, J., Liu, E., et al. (2011). Merra: NASA's modern-era retrospective analysis for research and applications. *Journal of Climate*, *24*, 3624–3648. https://doi.org/10.1175/Jcli-D-11-00015.1

Rotstayn, L. (1997). A physically based scheme for the treatment of stratiform clouds and precipitation in large-scale models. I: Description and evaluation of the microphysical processes. *Quarterly Journal of the Royal Meteorological Society*, *123*, 1227–1282. https://doi.org/10.1002/qj.49712354106

Rotstayn, L., Ryan, B., & Katzfey, J. (2000). A scheme for calculation of the liquid fraction in mixed-phase stratiform clouds in large-scale models. *Monthly Weather Review*, *128*, 1070–1088. https://doi.org/10.1175/1520-0493(2000)128<1070:asfcot>2.0.co;2

Seifert, A., & Beheng, K. (2005). A two-moment cloud microphysics parameterization for mixed-phase clouds. Part 1: Model description. *Meteorology and Atmospheric Physics*, *92*, 45–66. https://doi.org/10.1007/s00703-005-0112-4

Stephens, G., Li, J., Wild, M., Clayson, C., Loeb, N., Kato, S., et al. (2012). An update on Earth's energy balance in light of the latest global observations. *Nature Geoscience*, *5*, 691–696. https://doi.org/10.1038/Ngeo1580

Straka, J. (2009). *Cloud and precipitation microphysics*, Cambridge University Press. https://doi.org/10.1017/cbo9780511581168

Swales, D., Pincus, R., & Bodas-Salcedo, A. (2018). The cloud feedback model intercomparison project observational simulator package: Version 2. *Geoscientific Model Development*, *11*, 77–81. https://doi.org/10.5194/gmd-11-77-2018

Tiedtke, M. (1993). Representation of clouds in large-scale models. *Monthly Weather Review*, *121*, 3040–3061. https://doi.org/10.1175/1520-0493(1993)121<3040:rocils>2.0.co;2

Tong, M., Zhu, Y., Zhou, L., Liu, E., Chen, M., Liu, Q., & Lin, S. (2020). Multiple hydrometeors all-sky microwave radiance assimilation in fv3gfs. *Monthly Weather Review*, *148*, 2971–2995. https://doi.org/10.1175/Mwr-D-19-0231.1

Trenberth, K., Fasullo, J., & Kiehl, J. (2009). Earth's global energy budget. *Bulletin of the American Meteorological Society*, *90*, 311–323. https://doi.org/10.1175/2008bams2634.1

Tripoli, G., & Cotton, W. (1980). A numerical investigation of several factors contributing to the observed variable intensity of deep convection over South Florida. *Journal of Applied Meteorology*, *19*, 1037–1063. https://doi.org/10.1175/1520-0450(1980)019<1037:aniosf>2.0.co;2

Wild, M., Hakuba, M., Folini, D., Dorig-Ott, P., Schar, C., Kato, S., & Long, C. (2019). The cloud-free global energy balance and inferred cloud radiative effects: An assessment based on direct observations and climate models. *Climate Dynamics*, *52*, 4787–4812. https://doi.org/10.1007/s00382-018-4413-y

Wisner, C., Myers, C., & Orville, H. (1972). Numerical model of a hail-bearing cloud. *Journal of the Atmospheric Sciences*, *29*, 1160–1181. https://doi.org/10.1175/1520-0469(1972)029<1160:anmoah>2.0.co;2

Wu, W., & McFarquhar, G. (2016). On the impacts of different definitions of maximum dimension for nonspherical particles recorded by 2D imaging probes. *Journal of Atmospheric and Oceanic Technology*, *33*, 1057–1072. https://doi.org/10.1175/jtech-d-15-0177.1

Xu, K., & Randall, D. (1996). A semiempirical cloudiness parameterization for use in climate models. *Journal of the Atmospheric Sciences*, *53*, 3084–3102. https://doi.org/10.1175/1520-0469(1996)053<3084:ascpfu>2.0.co;2

Zhao, Q., Black, T., & Baldwin, M. (1997). Implementation of the cloud prediction scheme in the eta model at NCEP. *Weather and Forecasting*, *12*, 697–712. https://doi.org/10.1175/1520-0434(1997)012<0697:iotcps>2.0.co;2

Zhao, Q., & Carr, F. (1997). A prognostic cloud scheme for operational NWP models. *Monthly Weather Review*, *125*, 1931–1953. https://doi.org/10.1175/1520-0493(1997)125<1931:apcsfo>2.0.co;2

Zhou, L., Bao, Q., Liu, Y., Wu, G., Wang, W., Wang, X., et al. (2015). Global energy and water balance: Characteristics from finite-volume atmospheric model of the IAP/LASG (FAMIL1). *Journal of Advances in Modeling Earth Systems*, *7*, 1–20. https://doi.org/10.1002/2014ms000349

Zhou, L., Lin, S., Chen, J., Harris, L., Chen, X., & Rees, S. (2019). Toward convective-scale prediction within the next generation global prediction system. *Bulletin of the American Meteorological Society*, *100*, 1225–1243. https://doi.org/10.1175/Bams-D-17-0246.1